Morphological transformation of the process zone at the tip of a propagating crack. I. Simulation

Alexei Boulbitch*
Zum Waldeskühl 12, 54296 Igel, Germany

Alexander L. Korzhenevskii
Institute for Problems of Mechanical Engineering, RAS, Bol'shoi prosp. V. O. 61, 199178 St. Petersburg, Russia

(Received 8 December 2018; accepted 11 February 2020; published 11 March 2020)

Stress concentration at a crack tip engenders a process zone, a small domain containing a phase, different from that in the bulk of the solid. We demonstrate that this zone at the tip of a propagating crack exhibits a morphological transformation with an increase of the crack velocity. The concave zone shape with an invagination in its back that is characteristic of a slow crack transforms into a droplet-shaped convex zone upon exceeding a critical velocity value, v_G. In this latter case, a metastable wake follows the propagating zone. We obtained this result by computer simulation of a crack propagating in a solid exhibiting a first-order phase transformation.

DOI: 10.1103/PhysRevE.101.033003

I. INTRODUCTION

The traditional approach to the description of the fracture was developed in the first half of the last century. It was formulated in terms of simplified mathematical models of cracks as a generalization of macroscopic observations of the fracture. In brittle solids, the cracks were regarded as mathematical cuts in the otherwise homogeneous solid. In plastic ones, pertinent dislocation structures were added to the description (such as in the models of Barenblatt and Dugdale [1,2]).

However, new experimental data that emerged over the last few decades forces one to revise this point of view. The existence, at the tips of cracks, of small, nanometer- to micrometer-sized domains with specific properties (referred to as *process zones*) has been established in many materials previously assumed to be brittle. Within the process zones, linearity typically fails and dissipation takes place.

This progress is based on the employment of modern instruments of the last generation, such as high-resolution synchrotron scattering (HRTEM) [3], high-angle annular dark-field scanning transmission electron microscopy [4], electron nanodiffraction [5], scanning electron microscopy combined with electron backscatter diffraction [6,7], and high-resolution x-ray microdiffraction [8]. These techniques enable one to directly obtain the locations of the atoms.

In addition, methods providing an accurate determination of the configuration of the process zone have been developed, such as digital image correlation [9,10], Raman mapping [11], atomic force microscopy [12,13], infrared tomography [14], and nanoindentation [15], to name a few.

These methods demonstrate that the crystal structure of the process zone often differs from the one thereout. In this paper, the phase of the process zone we refer to as the *daughter phase*, while that of the matrix is referred to as the *mother phase*.

Transformations of the crystal structure within the process zone have been discovered in materials of various chemical compositions and crystal structures. It has been found in metals such as iron [16] and molybdenum [5], in steels [2,7,17], in the nitinol [8,9,18,19] as well as in other shape-memory alloys, such as Cu-Al-Ni [20], Cr-Ni [21], Ni-Al [22,23], and Ni-Mn-Ga [24], in titanium [25] and its alloys [26], as well as in metallic glasses [27].

In dielectrics this phenomenon has been observed in sapphire [28], in silicon [29], in ferroelectric monocrystals and ceramics [11,12,30,31], in diamonds [32], in the 2D nanocrystal molybdenum tungsten diselenide $MoWSe_2$ [33], as well as in high-T_c superconductors [34]. It has also been discovered in polymers [35] and in resins [36].

Computer simulations also reveal transformations of the crystal structure within the process zones. Such simulations have been reported to be performed for iron [37], silicon [38], titanium [39], tantalum [40], zirconium [41], UO_2 [42], and nitinol [43].

In early experiments on ZrO_2 [44,45], the transformational process zone has been detected by the so-called "postmortem" study. One observed a wake, a long-lived layer on the crack surface after fracture. The layer had the thickness in the micrometer range and contained a monoclinic phase, while the bulk of the solid consisted of the tetragonal phase. Before fracture, the ZrO_2 samples stayed in the tetragonal phase. More details on the observation of wakes can be found in the reviews [45–47]. Wakes have also been observed in PZT ceramics [30,31], in sapphire [28], in stishovite [48], in silica and borosilicate glass [49], under thermal fracture of diamonds [32], in polycrystalline silicon [50], in high-density polyethylene [51], in nitinol [52], in single crystals CuAlNi and Ni-Mn-Ga with the shape-memory effect [20,24], in TRIP

*Corresponding author: alexei.boulbitch@t-online.de

steels [53,54], in antiferroelectric ceramics [11], in polycrystalline ferroelectric PZT [55], in high-T_c superconductors YBCO and BSCCO [34], in metallic glass Zr-Ti-Cu-Nb-Be [56], and in the 2D crystal $MoWSe_2$ [33].

The direct electron microscope observation of the formation of a wake behind a propagating crack in a martensite-austenite alloy has been reported in [57], and it has been studied by mechano-luminiscence in ZrO_2 [58].

One has reliably established that the formation of the wake correlates with a considerable improvement of the solid fracture toughness, referred to as the *transformation toughness* [45], giving rise to a keen interest in this phenomenon.

Pioneered by McMeeking and Evans [59] and Budiansky [60] and followed by a large number of researchers [45], the formation of the process zone has been discussed within the continuum mechanical approach. This approach is based on three implicit assumptions: that the transformational process zone only differs from the rest of the solid by (i) its elastic modulus, (ii) the spontaneous strain engendered by the phase transformation, and (iii) that it can eventually divide into domains (in various communities also referred to as twins or variants). The continuum mechanical approach ignores all other degrees of freedom eventually describing the process zone.

The physical interpretation was as follows. The emergence of the daughter phase exhibiting a dilatation becomes energetically favorable under the influence of great stretching stresses. Therefore, it is thermodynamically stable at the tip of the crack, where such stresses are localized. In the course of the growth of the crack, the stress behind the tip vanishes. The material in this part of the zone finds itself in a metastable state. On the one hand, the energy of this metastable state contributes to the fracture energy, as was first discussed by Antolovich [61] to explain the transformation toughening effect in TRIP steels [2,45,53,62]. On the other hand, the less dense wake material generates compressive stress exerted on the crack surfaces. One should subtract the latter from the contribution of the external load to the stress intensity factor [59]. There is a long-lasting discussion of whether or not these two approaches represent the same mechanism [45]. Not entering this discussion let us observe that both mechanisms contribute to the fracture toughness, K_{IC}, in some materials the contribution being considerable. They, for example, yield the increase of K_{IC} in stishovite [48] and ZrO_2 [63] by an order of magnitude.

The formation of the transformational process zone in solids of various types along with the effect of the transformation toughening shows that it is a typical, rather than a specific, phenomenon. The universality of the existence of a process zone and its effect on the fracture toughness suggests that one should regard it within a universal theoretical approach.

One can divide brittle materials into two classes. The first of them consists of materials with the process zone, exhibiting an essentially elastic nonlinearity. Such a process zone exhibits a fast, nonlinear wave dynamics characterized by the (nonlinear) sound velocity, c. Since $V < c$ the zone behind the crack tip collapses, and the wake cannot develop. One observes such zones in brittle gels [64], polymers [35], resins [36], stishovite [48], ferroelastic crystals, and some martensites.

In the second class, another intrinsic degree of freedom, the order parameter, exhibits a nonlinearity, while the elastically nonlinear zone is small and can be disregarded. It is essential that the order parameter is different from the strain. Its dynamics is dissipative. Typically, it is slower than the sound velocity, and the wake can form. Most materials exhibiting local stress-induced phase transformations belong to the second class.

As an approach, enabling one to model process zones in the second class of materials, we have put forward a field-theoretical formalism regarding process zones as domains with local phase transitions [57,65–70]. For the description of the process zone, this formalism introduces an n-component field of the order parameter $\boldsymbol{\eta} = (\eta_1, \eta_2, \ldots, \eta_n)$. The latter is related to n degrees of freedom determining the difference in the crystal structure between the process zone and the matrix [69]. Let us stress that while in a small class of the so-called proper ferroelastic local phase transitions, some combinations of the strain tensor components, indeed, represent the order parameter, in all the other much more numerous cases the order parameter field is different from the strain tensor. In this case, the mentioned n-component degree of freedom represents a primary order parameter exhibiting its intrinsic static and dynamic behavior. The strain tensor, in this case, plays the role of the secondary order parameter that follows the primary one and modifies its effect. Together, they exhaustively describe the state and dynamics of the process zone.

In this paper we study the simplest case of a one-component order parameter ($n = 1$). In general, regarding the formation of the process zone, one recognizes that the local phase transitions often (though not always) correspond to the bulk phase transitions. That is, the phase diagram of the solid shows the mother phase, but also typically contains the same phase that shows up in the process zone, the daughter phase.

One classifies bulk phase transitions by their order. Second-order bulk phase transitions exhibit a continuous, piecewise smooth dependence of the order parameter on external thermodynamic quantities, such as the temperature $\eta = \eta(T)$. The point of discontinuity of the first derivative of the $\eta(T)$ dependence takes place at the Curie temperature T_c. However, one rarely meets true second-order phase transitions in nature.

Most phase transitions are first order [71]. First-order bulk transitions have a discontinuity of their order parameters $\eta = \eta(T)$ as the function of temperature at the point of the first-order phase transition. Besides, first-order phase transitions exhibit hysteresis, i.e., a region in the phase diagram of the solid in which two (or more) bulk phases can coexist, one of them being stable, and the others metastable. Typically, it has a width of about 1 to 10 K [71], although in some materials, such as metals exhibiting martensitic transformations, the hysteresis may be much wider [72].

The order of the bulk transitions, first order or second order, manifests itself in the behavior of the process zone. To highlight this correspondence, we specify below the *process zone engendered by the phase transition of the first or of the second order*, or merely, a *first or a second order zone*.

The zone engendered by a second-order transition emerges gradually with the increase of the stress intensity factor. Due

to its continuity, the description of the second-order zone is mathematically simple, admitting the application of bifurcation theory. The latter enabled us to develop its analytical theory [69].

What emerge at crack tips in a much larger number of solids are first-order zones. Such zones emerge stepwise and exhibit hysteresis. It is in this case that the formation of a metastable wake becomes possible.

One can address the first-order process zone exhibiting a metastable wake within the field-theoretical approach. In [70] we briefly reported the results of simulating the first-order process zone at the tip of a propagating crack. During the simulations, we observed that with increasing crack tip velocity the shape of the process zone changes, passing from concave to convex.

In this paper, we communicate a detailed analysis of this problem. We report simulations of the process zone at the tip of a crack propagating with a constant velocity, the zone being engendered by a first-order transition. We described the zone using the relaxation method of computation. In the case of the first-order zone it exhibited, however, peculiarities also discussed in this paper. We study the dynamic behavior of the process zone at different positions of the solid in its phase diagram and crack velocities. We demonstrate that the morphological transformation of the zone takes place at a specific velocity, V_{G}, depending on the position in the solid phase diagram. At small crack velocities, everywhere in the phase diagram, the process zone appears to be concave. Its shape resembles a distorted cardioid. A concave zone exhibits no wake. As soon as the velocity reaches V_{G}, the invagination in the zone vanishes. At this point, a morphological transformation of the zone takes place. Above this velocity, $V > V_{\mathrm{G}}$, the shape of the zone changes to one resembling a droplet. In this case, a metastable wake with an approximately triangular shape follows the zone. Upon exceeding a critical velocity, V_{cr}, the process zone vanishes, and a bare crack propagates at velocity $V > V_{\mathrm{cr}}$.

The paper is organized as follows. In Sec. II we discuss the equation of motion of a first-order process zone. In Sec. III we describe the phase diagram of the process zone and indicate the region where the formation of a wake is possible. It is in this region that we performed the simulations we report in Sec. IV. Section V is devoted to the discussion. Appendix A gives full details of the derivation of the equation solved in the paper. Appendix B discusses the peculiarities of the relaxation method met in this problem and lists the technical details of the simulations.

The present paper is the first part of our communication. In part II [73] we analyze the geometrical parameters obtained from our simulations, derive analytical relations for these parameters, and compare them with the simulation results. We further apply these relations to discuss the experimental data and classify possible scenarios of the propagation of a crack.

II. EQUATION OF MOTION FOR THE ORDER PARAMETER

A. Free energy and dissipation function

The evolution of the order parameter, $\eta = \eta(X, Y, t)$, over time gives rise to the energy dissipation described by the dissipation function $\mathfrak{D}$:

$$\mathfrak{D} = \frac{\kappa}{2}\int_{\Omega}\left(\frac{\partial\eta}{\partial t}\right)^2 d\Omega, \tag{1}$$

where κ is the kinetic constant and t is the time. Since both the order parameter and the displacement vector only depend on the in-plane coordinates X and Y and are Z independent the integration runs over the plane: $d\Omega = dX\,dY$, $\boldsymbol{R} = (X, Y)$ is the in-plane radius vector, Ω is the infinite plane. We assign all the bulk integrals used here to the unit length in the Z direction.

The dissipation function (1) corresponds to a quasibrittle solid, where deviations from ideal brittleness are only due to the phase transformation. Accordingly, the dissipation function includes no terms related to the strain rates. Thus, we assume that there is no dissipation due to plastic deformation.

The order parameter $\eta(\mathbf{R}, t) \neq 0$ contributes to the solid's free energy, $\mathfrak{F}$:

$$\mathfrak{F} = \mathfrak{F}_0 + \int_{\Omega}\Phi(\eta, \boldsymbol{\varepsilon})d\Omega, \tag{2}$$

where $\mathfrak{F}_0$ is the free energy of a plate containing a crack without a process zone, $\Phi = \Phi(\eta, \boldsymbol{\varepsilon})$ is the free energy density of the process zone, and $\boldsymbol{\varepsilon} \equiv \varepsilon_{ik}$ is the strain tensor:

$$\varepsilon_{ik} = \frac{1}{2}\left(\frac{\partial u_i}{\partial X_k} + \frac{\partial u_k}{\partial X_i}\right).$$

Here $u_i = u_i(X, Y, t)$, also denoted as $\mathbf{u}(\mathbf{R}, t)$, is the displacement vector. It should not be confused with the rescaled order parameter, $u(x, y, \tau)$, used in the following.

One can write down the free energy density in the following form:

$$\Phi(\eta, \boldsymbol{\varepsilon}) = \Phi_{\mathrm{pt}}(\eta) + \Phi_{\mathrm{el}}(\boldsymbol{\varepsilon}) + A\eta^2\varepsilon_{ii}. \tag{3}$$

Here the function $\Phi_{\mathrm{pt}}(\eta)$ denotes the part responsible for the phase transition. We address the simplest case, a phase transition described by a one-component order parameter, η. This case catches the essential features of the formation of a process zone. One can represent $\Phi_{\mathrm{pt}}(\eta)$ as a polynomial in terms of even powers of the order parameter and its gradient. Since we aim to describe a first-order transition, the polynomial is, at least, of the sixth order:

$$\Phi_{\mathrm{pt}} = \frac{g}{2}(\nabla\eta)^2 + \frac{\alpha}{2}\eta^2 + \frac{\beta_0}{4}\eta^4 + \frac{\gamma}{6}\eta^6. \tag{4}$$

Here $\nabla\eta$ is the order parameter gradient, while $g > 0$ and $\gamma > 0$ are the parameters of the Landau potential (2). If $\beta_0 < 0$ the potential (4) describes the first-order phase transition. We address this case in the present paper. Expression (4) coincides with the classical Landau potential describing a bulk phase transition. The Landau theory assumes that only the factor α depends on the temperature: $\alpha = \alpha_0(T - T_{\mathrm{c}})$, where $\alpha_0 > 0$ is a constant, T is the temperature, and T_{c} is the Curie temperature [74]. A derivation of the expansion (4) and its detailed discussion can be found in, e.g., [75].

$\Phi_{\mathrm{el}}(\boldsymbol{\varepsilon})$ is the elastic part of the free energy density, and here we use the elastically isotropic approximation:

$$\Phi_{\mathrm{el}} = \frac{E\sigma}{2(1+\sigma)(1-2\sigma)}\varepsilon_{ii}^2 + \frac{E}{2(1+\sigma)}\varepsilon_{ik}^2, \tag{5}$$

where E is Young's modulus, σ is the Poisson ratio (which should not be confused with the stress tensor $\boldsymbol{\sigma} \equiv \sigma_{ik}$), and $\mu = E/2(1+\sigma)$ is the shear modulus.

Finally, the contribution $A\eta^2\varepsilon_{ii}$ to (3) takes into account the interaction between the strain and order parameter fields. Let us note that the form of the interaction term $A\eta^2\varepsilon_{ii}$ in (3) implies that the phase transition only gives rise to a *spontaneous dilatation*. That is, a variation of its volume always follows the phase transition in the solid. Whether it is an increase in the volume or a decrease depends on the sign of the striction constant A. For $A > 0$, the process zone only emerges at a temperature below that of the bulk phase transition, while for $A < 0$, it emerges above the phase transition line [68]. It is this latter case, $A < 0$, that we focus on here. Within the process zone, a spontaneous dilatation generates stress referred to as *spontaneous stress*.

A spontaneous dilatation is always the case when the phase transition is described by a one-component order parameter, which is what we address in this paper. More complex cases involving a multicomponent order parameter and ones generating a spontaneous shear we considered elsewhere [69].

The parameters of the Landau potential g, α_0, β_0, T_c, and A related to the phase transformation together with the elastic constants E and σ constitute a set of material constants of the solid controlling its phase transformations and fracture behavior.

B. Equation of motion

The free energy (2) and the dissipation function (1) enable one to derive a system of equations of motion on the order parameter, $\eta(\mathbf{R}, t)$, and the displacement vector, $\mathbf{u}(\mathbf{R}, t)$. Making use of the elastic Green's function, one eliminates the variables $\mathbf{u}(\mathbf{R}, t)$ and its derivatives from the system resulting in a single dynamic equation in terms of $\eta(\mathbf{R}, t)$:

$$\kappa \frac{\partial \eta}{\partial t} = g\Delta\eta - [\alpha - U(\mathbf{R}, t)]\eta - \beta\eta^3 - \gamma\eta^5, \qquad (6)$$

where $U(\mathbf{R}, t)$ accounts for the effect on the order parameter of the strain field generated by the crack tip.

Let us study the crack propagating with a constant velocity, V. In this paper, we do not study conditions of formation of such a regime; neither are we interested in the analysis of the eventual formation of its instabilities. This limitation allows us to avoid considering the equation of the crack motion [76] and straightforwardly conclude that the strain tensor depends on coordinates and time as $\varepsilon_{ij}(\mathbf{R}, t) = \varepsilon_{ij}(X - Vt, Y)$.

We further assume $V \ll c$ which allows us to disregard "relativistic" corrections. Later on (in the discussion to part II of this work [73]), we justify this assumption by estimates of the characteristic velocities.

One finds

$$U(\mathbf{R}, t) = \frac{B\cos(\theta/2)}{[(X - Vt)^2 + Y^2]^{1/4}}, \qquad (7)$$

where $\theta = \arctan(Y/X)$ and

$$B = \frac{4|A|(1+\sigma)(1-2\sigma)K_I}{E\sqrt{2\pi}}. \qquad (8)$$

We refer the reader to Appendix A for details of the derivation of Eq. (6).

Equation (6) admits, however, a further simplification. Namely, one can pass from the independent dimensional variables $\mathbf{R}$, t and the dependent dimensional variable, $\eta(\mathbf{R}, t)$, to the dimensionless coordinates: x, y, and the dimensionless time, τ, as well as a dimensionless order parameter, $u = u(\mathbf{r}, \tau) = u(x - vt, y)$ (see Appendix A). One comes to the equation

$$\Delta u + 2^{1/3} v \times \frac{\partial u}{\partial x} - [a - \widetilde{U}(x, y)]u + bu^3 - u^5 = 0 \qquad (9)$$

with the boundary condition $u|_{\partial\Omega} = 0$. Here $\Delta u = \partial^2 u/\partial x^2 + \partial^2 u/\partial y^2$ is the Laplace operator in terms of the dimensionless coordinates x and y. The function $\widetilde{U}(x, y)$ describes the effect of the crack tip stress on the order parameter in the rescaled equation:

$$\widetilde{U}(x, y) = \frac{[(x^2 + y^2)^{1/2} + x]^{1/2}}{(x^2 + y^2)^{1/2}} \equiv \frac{\sqrt{2}\cos(\theta/2)}{\sqrt{r}}, \qquad (10)$$

where $r = \sqrt{x^2 + y^2}$ and $\theta = \arctan(y/x)$. The rescaled equation (9) only depends on three dimensionless control parameters, a, b, and the dimensionless velocity v. They are related to the original parameters as follows:

$$a = \frac{2^{2/3} g^{1/3}}{B^{4/3}}\alpha, \quad b = \frac{2^{1/3} g^{1/6}}{B^{2/3}\gamma^{1/2}}|\beta|, \quad v = \frac{\kappa}{(2g)^{1/3}B^{2/3}}V. \qquad (11)$$

Let us stress that formally Eq. (9) includes no dependence on time. For this reason, it is referred to as *static* in the following text.

Let us observe that formally one can obtain the equation of motion (9) from the dissipation function and free energy written in terms of the rescaled variables:

$$\mathfrak{D}' = \frac{1}{2}\int \left(\frac{\partial u}{\partial \tau}\right)^2 dxdy, \quad \mathfrak{F}' = \int \Phi_{\text{eff}}(u)dxdy. \qquad (12)$$

Its density, $\Phi_{\text{eff}}(u)$, has the form

$$\Phi_{\text{eff}}(u) = \tfrac{1}{2}(\nabla u)^2 + \tfrac{1}{2}[a - \widetilde{U}(x, y)]u^2 - \tfrac{1}{4}bu^4 + \tfrac{1}{6}u^6, \qquad (13)$$

where we always regard u as a function of the coordinates x and y. Further, ∇u is the dimensionless gradient of the rescaled order parameter: $\nabla u = (\partial u/\partial x, \partial u/\partial y)$.

III. THE BULK PHASE DIAGRAM

Let us briefly recall the bulk phase diagram of a solid with an unloaded crack ($B = 0$). It is generated by Φ_h, the homogeneous part of the free energy density, Φ_{eff} (13):

$$\Phi_h(u) = \tfrac{1}{2}au^2 - \tfrac{1}{4}bu^4 + \tfrac{1}{6}u^6, \qquad (14)$$

also referred to as the *Landau potential*. One can construct this phase diagram in the coordinates a and b. Both parameters can be regarded as functions of a pair of thermodynamic parameters, such as temperature, T, and Z, where Z can be any other thermodynamic parameter, such as the hydrostatic pressure, the concentration of a component in a solid solution, the electric or magnetic field intensity, and so on. Thus, the dependence $a(T, Z)$ and $b(T, Z)$ one can understand as a mapping of the plane (b, a) onto the plane (Z, T).

A standard analysis [75] of the potential (14) requires looking for its minimum: $\partial\Phi_h(u)/\partial u = 0$, $\partial^2\Phi_h(u)/\partial u^2 > 0$,

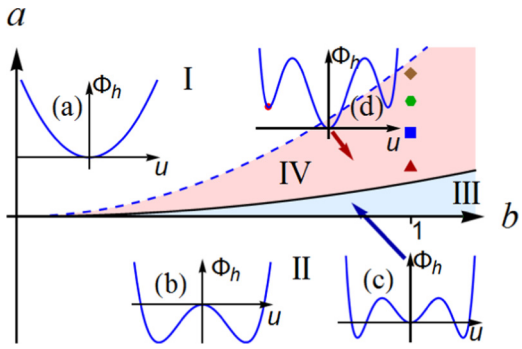

FIG. 1. Phase diagram of the Landau potential (14) in the (b, a) plane. The dashed line shows the upper spinodal (18); the solid black line is the binodal (20). The pure mother phase occupies region I, the pure daughter phase is situated within region II, while they coexist in the hysteresis regions III and IV (shaded). The insets show the dependence of the potential, $\Phi_h = \Phi_h(u)$. (a) and (b): In the mother and daughter phases, respectively. (c) and (d): In the hysteresis area. We placed dots at the points where the simulation has been done at $b = 1$ and $a = 0.24$ (diamond), 0.23 (hexagon), 0.22 (square), and 0.2 (triangle).

which yields the equation of state

$$au - bu^3 + u^5 = 0, \tag{15}$$

exhibiting three possible solutions. The trivial one describes the mother phase:

$$u_m = 0. \tag{16}$$

The two others describe the daughter phase:

$$u_d = \pm\sqrt{\frac{b + (b^2 - 4a)^{1/2}}{2}}. \tag{17}$$

This solution only exists as long as it corresponds to a minimum of the Landau potential ($\partial\Phi_h/\partial u = 0$, $\partial^2\Phi_h/\partial u^2 > 0$). As soon as this minimum transforms into the inflection point ($\partial\Phi_h/\partial u = \partial^2\Phi_h/\partial u^2 = 0$), the solution becomes unstable. The phase diagram line corresponding to the inflection point is referred to as the *spinodal*. The spinodals, therefore, bound the regions of the existence of the phases. One finds two such spinodals: upper and lower. The upper spinodal, $a = a_{up}(b)$, is expressed as

$$a_{up} = b^2/4. \tag{18}$$

It is shown by the dashed blue line in the phase diagram Fig. 1.

The lower spinodal, $a = a_{low}(b)$, has the form

$$a_{low} = 0. \tag{19}$$

In the phase diagram (Fig. 1), it is shown by the line coinciding with the b axis at $b > 0$.

Above the upper spinodal (region I in Fig. 1) the dependence of the Landau potential, Φ_h, on the order parameter, u, has a single minimum $u = 0$. This dependence is shown in the inset (a) in Fig. 1. This implies that only the mother phase exists for $a > a_{up}$. The Landau potential below the lower spinodal is shown in the inset (b) of Fig. 1. In this case, it only has minima (17) corresponding to the daughter phase. This means that for $a < 0$ (region II in Fig. 1), the mother phase does not exist.

Between these two lines (regions III and IV in Fig. 1) the Landau potential has a minimum at both $u = 0$ and $u = u_d$, as shown in Fig. 1, insets (c) and (d). This part of the phase diagram represents the hysteresis region, where the phases coexist.

One can find the condition that the mother and the daughter minima are equally pronounced, $\Phi_h(u_d) = \Phi_h(0)$, yielding

$$a_b = \frac{3b^2}{16}. \tag{20}$$

This line is referred to as the *binodal* or the *first-order transition line* by different communities.

Below this line, but above the lower spinodal (region III in Fig. 1), the minima of the daughter phase are more pronounced than the one of the mother phase [Fig. 1, inset (c)]. In this case, the daughter phase is thermodynamically stable, while the mother phase is metastable. Below a_b, the whole bulk of the solid transforms into the daughter phase. In this region, for $A < 0$ (the only case that we address in this paper), the order parameter distribution in the vicinity of the crack tip is, nevertheless, inhomogeneous. It, however, everywhere only corresponds to the daughter phase. Analysis of the inhomogeneous daughter phase is outside the scope of this paper.

In region IV in Fig. 1, for $a_b < a < a_{up}$ the minimum $u = 0$ corresponding to the mother phase is more pronounced than those (17) describing the daughter phase. In this case, it is the mother phase that is stable, while the daughter phase is metastable.

The phase diagram Fig. 1 was discussed above in terms of the dimensionless parameters a and b to bring it into accordance with the solution of Eq. (9) depending on the same parameters. Let us, however, note that the phase diagram in the parameters $(-\beta, \alpha)$ of the original Landau potential (4) has qualitatively the same form, with the upper spinodal expressed by $\alpha = \beta^2/4\gamma$, the lower spinodal by $\alpha = 0$, and the binodal by $\alpha = 3\beta^2/16\gamma$.

In this paper, we study the propagation of a crack in a solid that dwells in region IV of the phase diagram, where the daughter phase can only exist in a metastable state. In all calculations we put $b = 1$. With this value the upper spinodal $a_{up} = 0.25$, while the binodal value is $a_b = 3/16 \approx 0.188$. The dots in Fig. 1 at $b = 1$ show the points at the different values of a at which the simulations have been done: $a = 0.24$ (the blue disk), 0.23 (the green diamond), 0.22 (the red square), and 0.2 (the brown triangle), the first point lying close to the upper spinodal, while the last lies close to the binodal.

IV. PROCESS ZONE AT THE TIP OF A CRACK

We simulated Eq. (9) using the relaxation method (see Appendix B) with the finite-element method applying the COMSOL 5.3 software. We took $b = 1$ and multiple values of the dimensionless velocity, v, in the interval $0 \leqslant v \leqslant 1.2$, while the parameter a takes four values: 0.2, 0.22, 0.23, and 0.24. The results for all these values of a qualitatively resemble one another, only differing in size and proportion. For this reason, in most cases, we show the images obtained with $a = 0.24$, for various v.

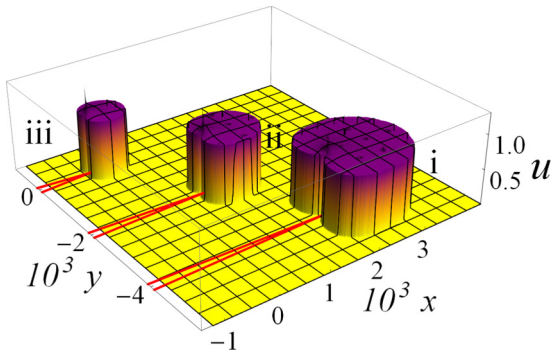

FIG. 2. Process zone at the tip of the motionless crack at various a values: (i) $a = 0.22$, (ii) $a = 0.23$, and (iii) $a = 0.24$.

A. A zone at the tip of the motionless crack

Figure 2 shows the process zones at the tips of the motionless cracks at $a = 0.22$ (i), 0.23 (ii), and 0.24 (iii). The straight lines behind the zone indicate the position of the crack surfaces. We have shown the zones close to one another to enable the comparison of their shapes and configurations.

Here and in the following the coordinates x and y in Fig. 2 are given in dimensionless units. One dimensionless unit corresponds to the characteristic length λ_0 (see Appendix A). One finds estimates of the possible value of the characteristic length along with discussion in part II [73].

One observes that the zone size strongly depends on the value of the parameter a and rapidly increases upon approaching the binodal. Let us point out an invagination in the rear part of the zone where the zone meets the crack surfaces.

Figure 3(a) shows the contour of the process zone at the tip of the motionless crack within the example of $a = 0.24$. We obtained the contour as points of the crest of the distribution $(\nabla u)^2$ corresponding to the middle of the kink. Though on a large scale the zone shape closely resembles a cardioid, it differs from the latter in fine details. Especially important is the shape of the contour in the rear part of the interface, close to the crack surface [Fig. 3(b)]. In the case $a = 0.24$ it meets the crack surface ($y = 0$) at $x \approx -18.85$, rather than at $x = 0$, as should take place in the case of the cardioid. The analogous situation takes place also for other a values. In all cases we observed a finite setback $x < 0$. In detail the setback at $v = 0$ is summarized in part II [73].

B. A slowly propagating crack

Figure 4 shows the process zones at the tips of slowly propagating cracks at $a = 0.22$ (i), 0.23 (ii), and 0.24 (iii). Since the shapes of the zones strongly depend on a, we have chosen different velocities such that the zones' shape corresponds to those typical for the small crack tip speed. Thus, the zone indicated by (i) propagates with the velocity $v = 0.08$, while those marked by (ii) and (iii) move with $v = 0.16$.

We have chosen the view enabling one to better see the invaginations in the rear part of the zones considerably increased in comparison with the motionless crack-zone complex.

Figure 5 shows the example of the evolution with increasing the velocity, v, of the spatial distribution of the

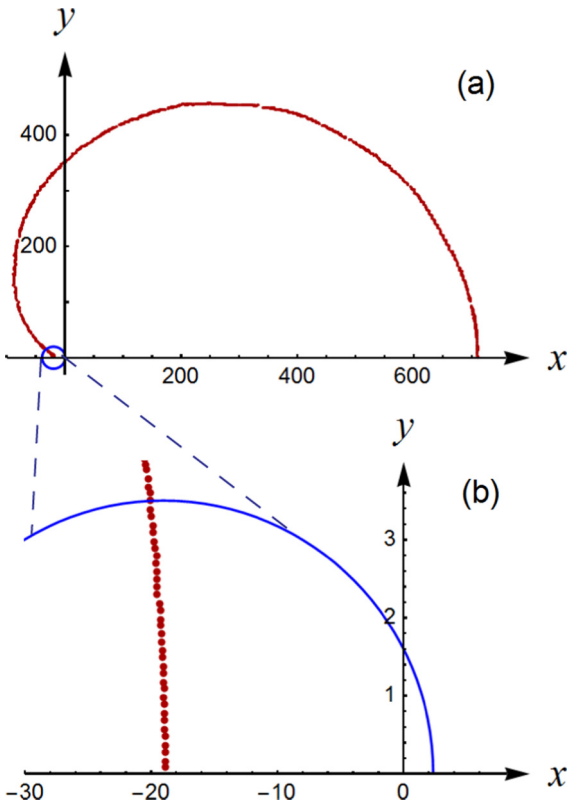

FIG. 3. (a) The contour of the interface of the motionless process zone ($a = 0.24$). Only the upper semiplane is shown. Red dots indicate the points of the contour corresponding to the points of the crest of $(\nabla u)^2$. The blue circle indicates the rear part of the contour. (b) The blown-up view of the rear part of the same contour in the close vicinity of the x axis.

dimensionless order parameter, u, at $a = 0.24$. Figure 5(a) shows the zone at the tip of a motionless crack, while panels (b)–(d) display those for the crack with a gradually increasing velocity. The crack spans along the semi-infinite line $y = 0$, $-\infty < x - v\tau \leqslant 0$, with its tip in the origin of the coordinates. The velocities of the crack propagation for the order parameter distributions shown in Fig. 5 are (a) $v = 0$, (b) $v = 0.159$, (c) $v = 0.238$, and (d) $v = 0.254$. As will be clear later, all of these are below the velocity corresponding to

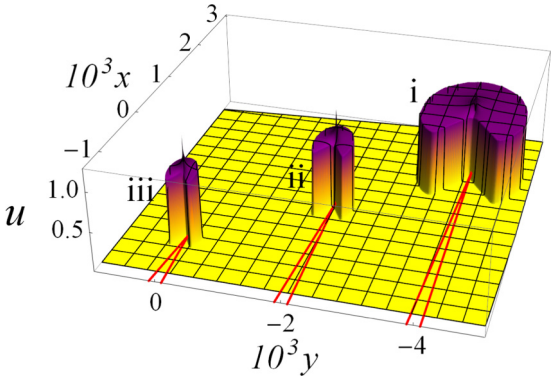

FIG. 4. Process zones at the tips of slowly propagating cracks at various a values: (i) $a = 0.22$, (ii) $a = 0.23$, and (iii) $a = 0.24$.

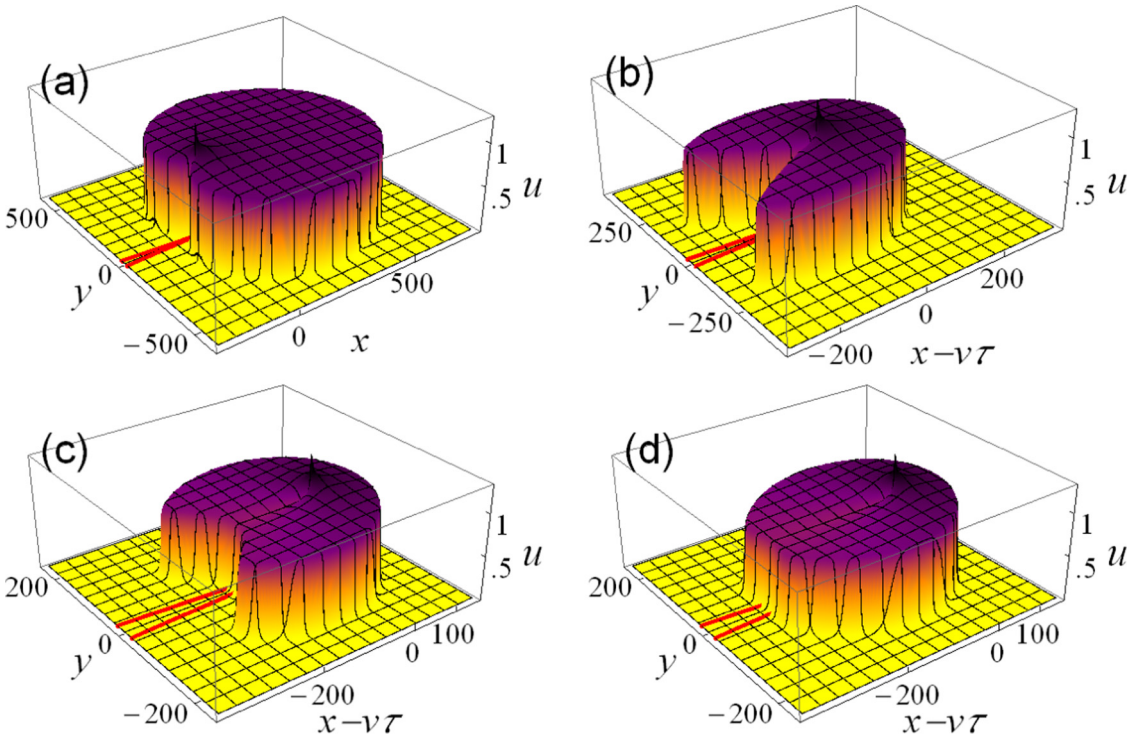

FIG. 5. The distribution of the order parameter, $u(x - v\tau, y)$, within the process zone at $a = 0.24$, $b = 1$, and (a) $v = 0$, (b) $v = 0.159$, (c) $v = 0.238$, and (d) $v = 0.254$. The red lines behind the distribution schematically indicate the positions of the crack surfaces.

the morphological transformation, v_G, the velocity $v = 0.254$ [Fig. 5(d)] being only slightly smaller than v_G.

The simulation results show the following general properties of the order parameter distribution in the vicinity of the crack tip characterizing a first-order process zone: Far from the process zone, the order parameter is zero. At the boundary of the zone, it exhibits a steep kink passing into an almost plane "roof" [Figs. 5(a)–5(d)]. Figure 6(a) shows a cross section of all the order parameter distributions displayed in Fig. 5. The cross section is made along the plane $y = 0$. One can distinguish two different "roofs." One of them, indicated by the arrow α in Fig. 6(a), belongs to the leading zone part. This leading roof, with a height, u_1, between 0.79 and 1.2, has a shallow slope of $\sim 10^{-3}$ to $\sim 10^{-4}$. The former estimate of the slope we obtained in the case of the steepest, narrowest zone, while the latter one is for the case of the widest, most shallow one. That is, the order parameter in this region gently increases with decreasing distance to the crack tip at (0,0). In most of this region, it does not exceed $u = 1$. A peak reaching the value of $u = 1.2$ is visible in the close vicinity of the crack tip.

The roof, indicated by the arrow β, is situated behind the crack tip. It thus belongs to the trailing part of the zone. It forms an almost flat plateau with a height of $u_2 \approx 0.8$ and negligibly small slope. Let us stress that the values u_1 and u_2 given above are valid for $a = 0.24$. In general, u_1 and u_2 depend on a and b, as we discuss in detail in part II [73].

Figure 6(a) also shows that the heights, $u_{1,2}$, of the roof are not sensitive to the speed of the tip of the crack. The size of the zone, in contrast, decreases with increasing velocity of the crack tip. The latter is visible in Fig. 6(b), where we show the zone boundaries in the upper half plane $y > 0$.

At low crack tip speeds, the zone contour represents a deformed cardioid, as if the process zone at a motionless

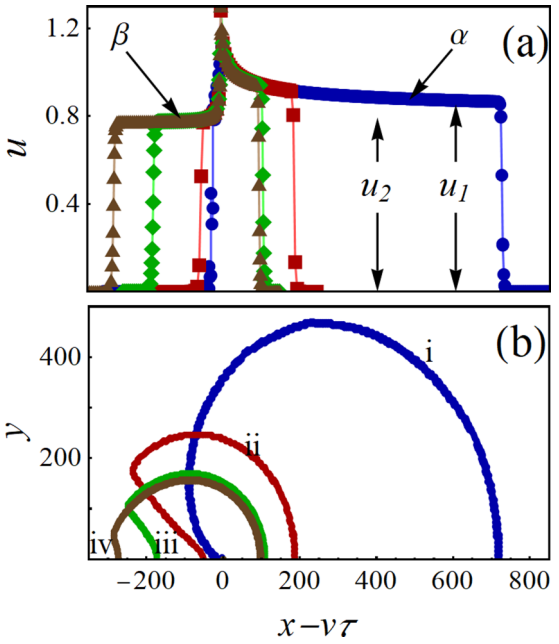

FIG. 6. (a) A cross section of the zone along the line $y = 0$ at $a = 0.24$, $b = 1$. The arrow α indicates the "roof" of the leading part of the distribution with the height u_1, while β points out its trailing part. Here the roof height is u_2. (b) The zone boundary in the upper half plane $y > 0$. The circles [panel (a)] and the contour (i) [panel (b)] correspond to the velocity value $v = 0$, the squares and contour (ii) to 0.159, the diamonds and contour (iii) to 0.238, and the triangles and contour (iv) to 0.254.

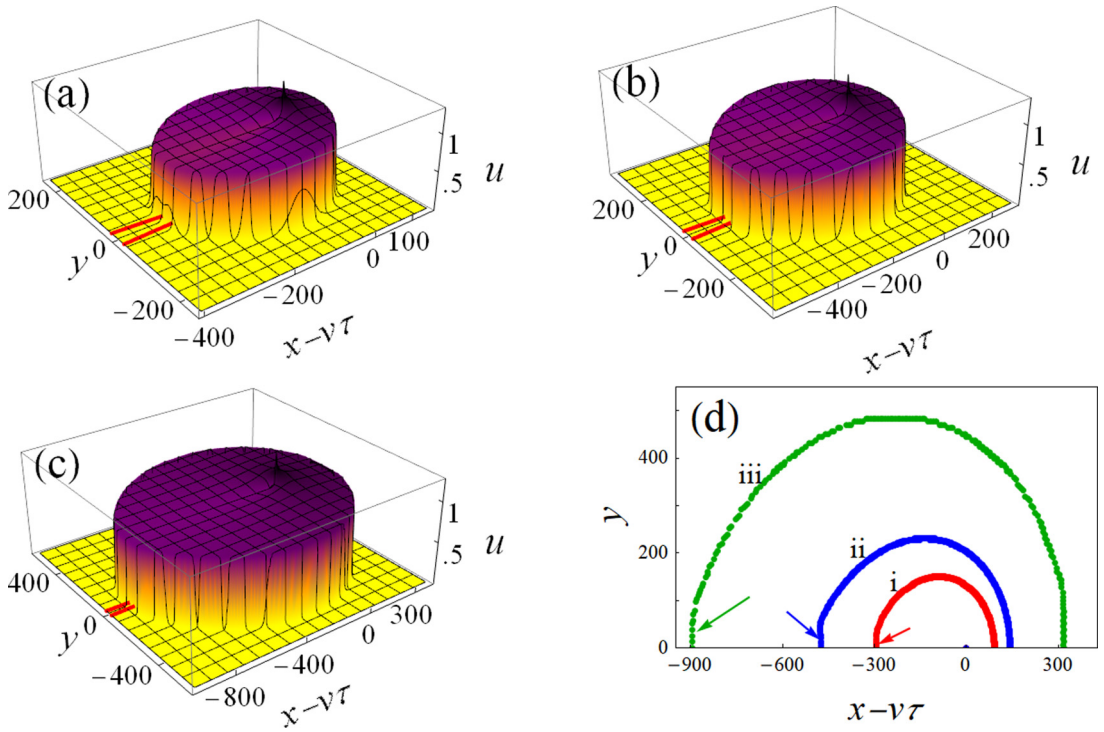

FIG. 7. (a)–(c) Order parameter distribution at the tip of a crack propagating with the velocity of the morphological transformation, v_G, equal to 0.264 at $a = 0.24$ (a), 0.22 at $a = 0.23$ (b), and 0.149 at $a = 0.22$ (c). The red lines behind the distribution schematically show the position of the crack surfaces. (d) The zone boundary contours (at $y > 0$) of the zones propagating with the transformation velocities: (i) corresponds to the image (a), (ii) to (b), and (iii) to (c). The arrows indicate the end of the trailing zone, where the zone boundary is perpendicular to the y axis.

crack tip were decreased in its size and stretched somewhat backward. The point where the zone boundary hits the crack surface, $y = 0$, is also shifted backward to some value at $(-l, 0)$, the distance $l = l(v)$ increasing with the velocity. The zone exhibits an invagination in its rear part. The depth of the invagination, however, depends on the crack tip velocity, and gradually vanishes upon approaching v_G [see Fig. 6(b), contour (iv)].

To avoid a misunderstanding, let us make it clear that the distribution shown in Fig. 6(a) is taken along the line $y = 0$ and, thus, passes through the invagination. The end point of the roof β shown in Fig. 6(a) is taken at the crack surface and has the coordinates $(-l, 0)$. It lies behind the crack tip $x - v\tau = 0$, $y = 0$. The length $l > 0$ is equal to the distance from the deepest point of the invagination $(-l, 0)$ to the crack tip (0,0). In contrast, the size of the distribution's "petals" may be greater, and the x projection of the coordinate of the back point of the petal, x_a, of the distribution is larger than l in its absolute value, as can be made clear by comparing Fig. 6(a) with Fig. 6(b).

C. The morphological transition

As soon as the crack tip velocity reaches a certain value, v_G, the order parameter distribution loses its concavity. The back part of the zone boundary becomes perpendicular to the y axis. In the cases of $a = 0.22$, 0.23, and 0.24 the distribution $u(x - v\tau, y)$ is shown in Figs. 7(a)–7(c). It is at this value of the crack tip velocity that the morphological transformation takes place.

The velocities of the morphological transformation, v_G, depend on the place on the phase diagram. Since we fixed $b = 1$ this manifests itself in the dependence on a. We summarize the values $v_G(a)$ in Table I.

Figure 7(d) displays the boundaries of zones propagating with the velocities of the morphological transformation for the cases shown in Figs. 7(a)–7(c). The arrows indicate the rear portions of the boundaries, where they are flat and normal to the y axis.

D. Process zone at the tip of a fast-propagating crack

As soon as the velocity exceeds v_G, the zone becomes convex. Figure 8 shows the overcritical configurations of the process zone at different velocities. The zone takes the form of a droplet with a pointed end. This droplet is considerably stretched out along the x axis.

The dependence of the geometry of the zone on the velocity of the crack tip is visible in Fig. 9(a), which shows the contours of the process zone for the order parameter distributions displayed in Figs. 9(a)–9(d). The contour (i) corresponds to Fig. 9(a), the contour (ii) to (b), (iii) to (c), and (iv) to (d). One can see that the size of the zone decreases with increasing velocity.

TABLE I. Velocities of the morphological transition.

a	0.22	0.23	0.24
v_G	0.149	0.220	0.264

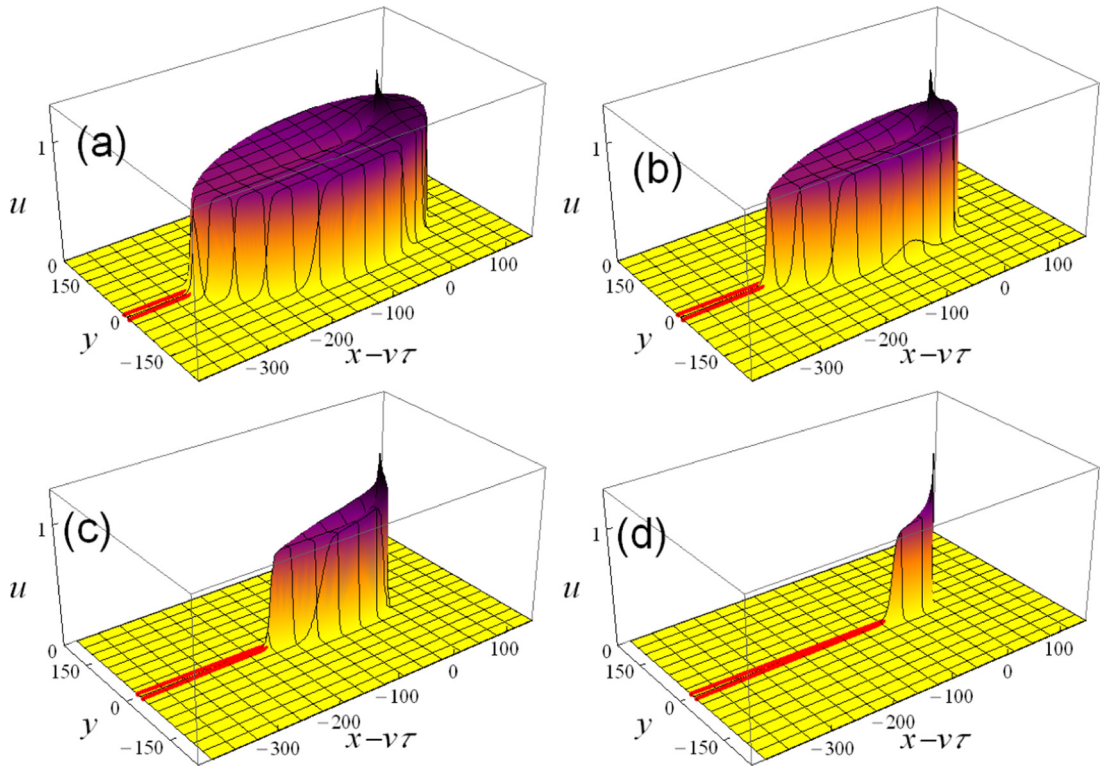

FIG. 8. Order parameter distribution around the tip of a crack propagating with velocity exceeding v_G. The simulation results with $a = 0.24$, $b = 1$ are shown. The panel (a) shows the configuration slightly above the transition $v \approx 0.294$, (b) $v \approx 0.4$, (c) $v \approx 0.63$, and (d) shows the distribution at $v \approx 1.03$, close to the critical velocity at which the zone vanishes. The solid red lines schematically indicate the position of the crack surfaces.

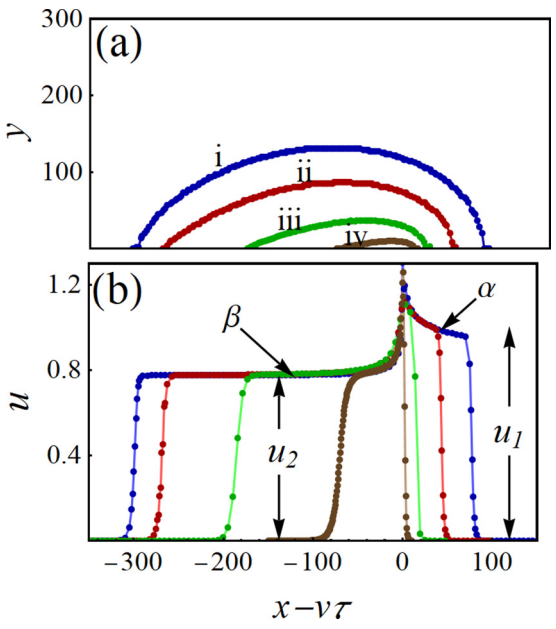

FIG. 9. (a) The boundaries of the process zones shown in Fig. 8. (b) Cross sections of the distributions of the order parameter shown in Fig. 8 along the crack ($y = 0$). α indicates the "roof" with height u_1 in front of the crack tip, and β indicates the one with height u_2 behind it. The distribution shown in Fig. 8(a) corresponds to the line indicated by (i), (b) to that indicated by (ii), (c) to that by (iii), and (d) corresponds to (iv).

As in the previous case, one finds a distribution with two roofs: the one indicated by the arrow α [Fig. 9(b)] has a height of $u_1 \approx 0.99$, is located in front of the crack tip, and exhibits a small slope varying between 5×10^{-3} and 2×10^{-2}. This slope only becomes pronounced, forming a small peak, in close vicinity ($0 \leqslant x - v\tau \lesssim 10$) to the crack tip. The rear roof (indicated by the arrow β) has a height of $u_2 \approx 0.776$ and a negligibly small slope of $\sim 10^{-4}$ up to the kink region.

It is also essential to understand how the configurations of the order parameter distributions vary depending on the place in the phase diagram at a fixed velocity. Figure 10 shows such distributions obtained with the velocity $v \approx 0.79$. We placed the distributions close to one another for comparison. One can see that for a approaching the binodal, the dimension of the distribution in the x direction dramatically increases. Some limited growth takes place also with the so-called *zone height* traditionally understood as the maximum zone dimension in the y direction.

To understand, how the roofs of the distributions depend on the distance $a - a_b$ from the binodal, it is convenient to analyze the cross sections of the order parameter distributions shown in Fig. 10. Figure 11 displays such cross sections.

One can see that in approaching the binodal, the roof height, u_2, slightly increases, which we summarize in the second line of Table II.

The second line of Table II shows the values of the roof height, u_2, at the rear part of the distribution for various values of the parameter a. One observes that values of u_2 are independent of the velocity. The third line of the same table

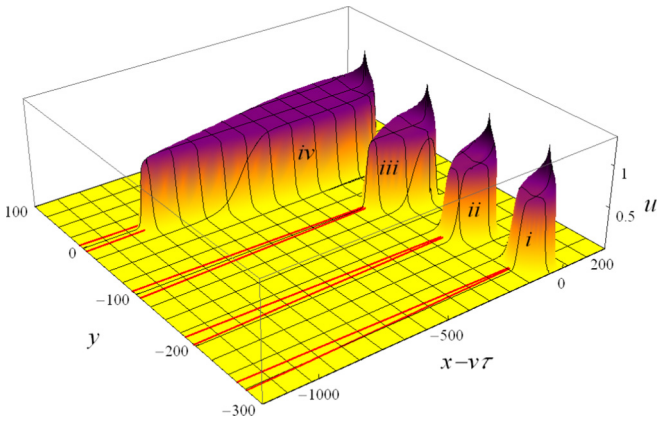

FIG. 10. Comparison of the configurations of the zone-wake complexes propagating with the same velocity exceeding v_G but at different distances from the binodal. (i) $a = 0.24$, (ii) $a = 0.23$, (iii) $a = 0.22$, and (iv) $a = 0.20$. Approaching the binodal, $a_b \approx 0.18$, the length of the wake dramatically increases, the "roof" height of the $u = u(x - v\tau, y)$ distribution staying the same. The solid red lines indicate the positions of the surfaces of the cracks.

presents the values of the order parameter in the daughter phase (17) at $b = 1$ for various a. One finds a close agreement between u_2 and u_d.

E. The width of the phase boundaries

Another interesting question is the width of the interface boundaries. The latter one can study by observing the behavior of $(\nabla u)^2$ which is close to zero everywhere, except the close vicinity to the kink. At the kink, the function $(\nabla u)^2$ exhibits a bell-shaped function.

Figure 12 shows the behavior of $(\nabla u)^2$ in the utmost leading zone part for $a = 0.24$ for different velocities: $v = 0.24$, 0.40, 0.56, 0.79, and 0.95. We fitted the points obtained from the simulation by the Gaussian curve. The fitting yields the wall thicknesses $d \approx 3.66$, 3.26, 3.94, 2.36, and 2.26 correspondingly. One concludes that the wall thickness is always much more narrow than the zone size. The same situation takes place in the cases of other a values.

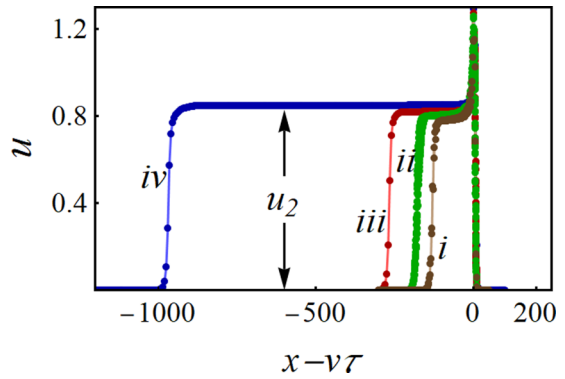

FIG. 11. Cross section of the order parameter distributions shown in Fig. 10 along the line $y = 0$. (i) $a = 0.24$, (ii) $a = 0.23$, (iii) $a = 0.22$, and (iv) $a = 0.20$.

TABLE II. Variation of the "roof" height.

a	0.2	0.22	0.23	0.24
u_2	0.85	0.82	0.81	0.79
u_d	0.85	0.82	0.80	0.78

F. The critical velocity

As soon as the velocity exceeds a certain value, v_{cr}, the process zone vanishes stepwise. Figure 13 compares three zone-wake complexes for the same value of $a = 0.2$ with three gradually increasing values of the velocity: (a) $v = 1.032$, (b) 1.111, and (c) 1.184. The last is the closest to the critical velocity value that we succeeded in obtaining. Under a further velocity increase, the solution is within the numerical noise. One can see that with the increase of the velocity from $v = 1.032$ to $v = 1.184$, the wake length, l, dramatically decreases. The zone height, h, and width, $\mathfrak{r}$, also decrease, although not as much as the wake length. It is important to note that the height of the $u(x - v\tau, y)$ distribution exhibits no variation up to the critical velocity.

V. DISCUSSION

A. Field-theoretical description of the process zone

One can only regard the process zone as a specific domain provided some of its properties differ from those in bulk. The process zone often exhibits a qualitative difference from the bulk, such as the difference in its chemical composition, its crystal structure (for example, cubic, tetragonal, or monoclinic lattice structures as in the case of ZrO_2 [45]), its electronic structure (such as metal or isolator as in VO_2, exciton condensate or exciton gas, normal or superconductive states [34]), or its magnetic structure (paramagnetic, ferromagnetic, antiferromagnetic). All the above structures (as well as those we did not mention here) are related to internal degrees of freedom. They activate locally in the vicinity of the crack tip due to the high stress.

One can divide all such internal degrees of freedom into two classes. To the first class belong the ones characterized

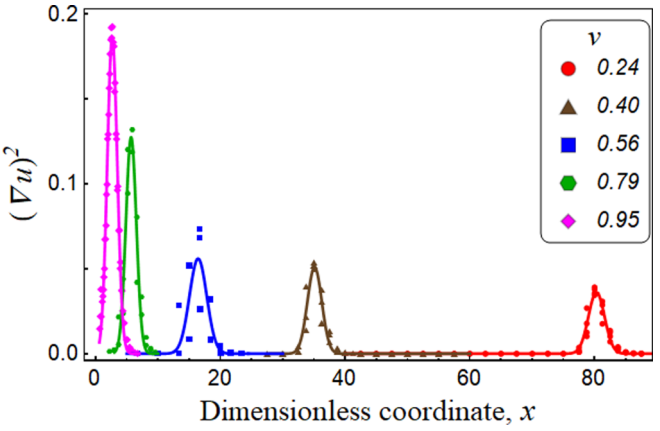

FIG. 12. The behavior of the $(\nabla u)^2$ along the line $y = 0$ in the leading zone part. The dots show the simulation results, while the solid lines display their fitting by the Gaussian curve.

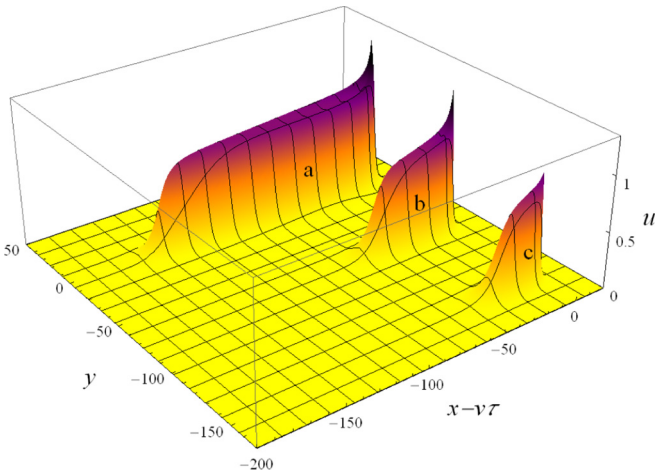

FIG. 13. The gradual variation of the process zone–wake complex in the vicinity of the critical point at $a = 0.24$. (a) $v \approx 1.032$, (b) $v \approx 1.111$, and (c) $v \approx 1.184$. A further increase of v gives rise to a dramatic vanishing of u, so that it is not visible in the plot.

by a potential, such as the Landau potential. The latter plays the role of the Lyapunov function for the dynamics of these degrees of freedom. The structural degrees of freedom, such as optical and acoustic phonons, magnons, degrees of freedom related to the electronic subsystem, belong to the first class. The degrees of freedom whose dynamics cannot be related to any potential belong to the second class, like those describing chemical reactions or plasticity. Derivation of equations describing the system belonging to these two classes requires different approaches.

In this paper, we only discuss the first class. Namely, we only consider the zones that differ from the bulk of the solid by the structure of its crystal lattice. To describe such a structural difference, Landau proposed [74] to introduce the order parameter, η. One constructs it as a set of degrees of freedom of the solid, such as normal coordinates of optical phonons. Our approach, therefore, is akin to the theory of structural phase transitions [74,77].

As in the Landau theory, one analyzes the solid phase diagram. The latter, in general, contains several phases. Let us denote the symmetry groups of their crystal lattices as $G, G_1, G_2, \ldots, G_m$, where m is an integer number $m \geqslant 1$. Further, the groups G_i are in a group-subgroup relation with the supergroup G: $G_i \subset G\,(i = 1, \ldots, m)$. Landau argued [74] that the order parameter transforms according to one of the irreducible representations of the supergroup G. The latter completely defines the order parameter [74] and the so-called Landau potential [77].

In accord with this, we describe the zone by the field, $\eta = \eta(r, t)$. Assuming $\eta \neq 0$ inside the zone while vanishing outside, one describes the zone with the symmetry group G_i and the matrix with the group G. If $\eta \neq 0$ in the matrix, it corresponds to one of the low-symmetry phases, G_i. At the same time, $\eta = 0$, within the zone, means that it contains the high-symmetry phase, G.

Let us also point out a few situations one should expect in the case of a multicomponent order parameter. On the one hand, one can face a situation with some order parameter components different from zero in the matrix, while some its other components are nonzero within the zone. Such a situation corresponds to the low-symmetry phases G_i and G_j $(i \neq j)$ describing the matrix and the zone or, in some cases, different domains (twins, or variants) of the same phase, G_i. On the other hand, one can meet a situation in which the zone consists of several subdomains, each containing another phase, $G_1, G_2, \ldots$.

A family of the so-called reconstructive transitions, such as transformations between body-centered cubic (bcc) and face-centered cubic (fcc) or hexagonal close-packed (hcp) structures, exhibits no such group-subgroup relation as discussed above. For a long time, therefore, the scientific community believed that, in this case, one could not apply the Landau theory. However, the introduction of a transcendental order parameter [78] demonstrated that Landau's theory could also efficiently cope with reconstructive transformations [79]. The process zone also can be of a reconstructive type. The observations of the fcc-bcc zone-matrix combination was reported in molybdenum [5] and in steel [7], and the bcc-hcp combination in iron [80] and in titanium [39].

All the zones described above are nonlinear. However, if one can regard the elasticity in such systems as a linear one, the nonlinearity in these cases is only related to the order parameter. This condition holds for many brittle solids. In this case, the field-theoretical approach offers a relatively simple description of the process zone.

Let us turn now to the cases that are not amenable to the field-theoretical approach.

Proper ferroelastic materials constitute a stand-alone class. They exhibit phase transformations described by the order parameter built out of components of the strain tensor [81]. In this case, one can still formulate the order-parameter-based theory of the process zone. The latter, however, represents equations of nonlinear elasticity, the nonlinearity being essential. One can only study these equations numerically. Even that can become, however, impossible since one typically measures the elastic modules of the higher orders with a significant scattering [82].

A similar problem arises at the description of process zones experiencing the local martensitic transformations accompanied by a high spontaneous strain. In these cases, one often can describe the transition by the structural order parameter, different from the strain tensor. However, high spontaneous strains make the problem highly elastically nonlinear. The situation is not much easier to deal with in a purely elastically nonlinear process zone (for instance, in brittle gels [64]). In all these cases, our approach offers no advantage.

From this discussion, one can see that the field-theoretical approach enables one to describe many process zones of very different origins uniquely by the introduction of an order parameter field, or several such fields.

The introduction of the order parameter as an "indicator field" of the process zone seems to be a promising idea even if the Landau potential does not exist. For example, one can introduce such an indicator field for zones involving local stress-induced chemical reactions, or those with dense dislocation pileups. One can, further, combine such an indicator field describing the extended process zone with the traditional phase-field order parameter [83], bringing the method high flexibility. A combination of the phase-field description of

cracks with the order-parameter-based description of the process zone may be a useful extension of both directions.

As for the difficulties, they are related to the fact that the Landau potential is a polynomial. It must provide it to be positively defined. That is, it is at least of the fourth order in the case of the second-order transformation, and at least of the sixth-order for the first-order one. However, in specific cases, the polynomial order may still occur higher. As a result, it may depend on many coefficients [such as α, β, and γ in Eq. (4)]. To get quantitative results for specific materials, one has to know the numerical values of such parameters. These, however, have been measured experimentally for a limited list of materials only [84].

B. Resumé

The equation of motion (9) exhibits a bifurcation [68] at $a = a_*$. For $a < a_*$, a process zone occupied by the daughter phase exists at the crack tip. For the potential (10) used here, this value is equal to $a_* = 2^{-2/3} \approx 0.63$.

In this paper, we only addressed the domain below the upper spinodal and only made our simulations with $b = 1$. These limitations prescribe the values of the parameter a to lie between $1/4$ (the upper spinodal) and $3/16$ (the binodal). These values lie well below $a_* \approx 0.63$. For this reason, we only dealt with the subcritical behavior of the equation of motion, and the process zone always existed in our simulations. Thus, in this paper, we are not interested in the emergence of the process zone. Our study focuses on configurations exhibited by an already existing, propagating process zone.

In the course of the simulation, we observed that at small crack tip speeds, the process zone is concave, with an invagination in its back. As soon as the velocity exceeds the value, v_G, the shape of the zone changes to be convex, taking a droplet configuration.

We established that a close coincidence takes place between the roof of the rear zone part, u_2, and the order parameter value, u_d, in the free, bulk daughter phase.

This is, however, not the case in the leading part of the distribution. The origin of the difference between the roof height in the leading and rear zone parts is that the leading part of the distribution belongs to the region where the potential, $U(r,\theta) = \sqrt{2}\cos(\theta/2)r^{-1/2}$, in Eq. (9) is considerable. It is this potential that determines the configuration of the leading part of the distribution.

Furthermore, if the crack is loaded ($K_I \neq 0$), but still motionless ($K_I < K_{IC}$), the zone is occupied by the daughter phase which is stable and can exist infinitely long. It is thermodynamically stabilized by the potential, $U(r,\theta)$. As soon as the crack moves, it is the propagation of this potential in front of the crack tip that forces the mother phase to transform into the daughter phase along the leading zone interface.

In contrast, behind the crack tip, the potential gradually vanishes, due to its angular dependence. Besides, in the case of u distributions stretched out over long distances (such as those displayed in Figs. 8 and 10) the effect of the potential in the rear part becomes negligible because it decreases as $\sim r^{-1/2}$.

One concludes that the daughter phase occupies the rear part of the distribution. Here, however, it is not stabilized by the potential, $U(r,\theta)$.

We only simulated the problem in region IV of the material bulk phase diagram (Fig. 1). As we discussed in Sec. III, in this region the free daughter phase is metastable. One concludes that the rear part of the order parameter distribution consists of the daughter phase in the metastable state. As soon as it is not stabilized, such a state gradually decays. In the case of a motionless crack, it has enough time for the whole metastable phase to vanish.

However, for $0 < v < v_G$ one observes that only small portions of the backward petals of the concave zone consist of the metastable daughter phase, while the rest of the zone is stable. It is stabilized by the potential $U(r,\theta)$.

Historically, it was the elongated "tail" of the daughter phase behind the propagating zone that one referred to as the *wake*. That is, the wake only forms for $v > v_G$, when the zone takes a convex, elongated, droplet-like shape. In this case, the daughter phase within the tail is not stabilized by the potential and exhibits a roof, u_2, almost equal to u_d, suggesting that it dwells in the metastable daughter phase.

Let us stress that as observed from our simulations, the whole wake travels together with the zone–crack tip complex, rather than staying behind forever. In other words, the backward wake point has the same velocity, v, as that of the crack tip. One concludes that the wake studied in this simulation differs from the infinitely long-lived one reported in early experiments [44], but rather is like the more recently observed ones [57,58]. The origin of these differences along with a detailed analysis of the wake parameters will be discussed in part II of the present paper [73].

The knowledge of the geometry of the process zone is a necessary basis for calculating the value of the stress intensity factor. The discovered morphological transformation inevitably influences the amount of the dynamic screening of the stress field at the crack. The latter affects the crack dynamics. The description of this dynamics is, however, out of the scope of this paper. This question we will address in a forthcoming paper.

VI. SUMMARY

To summarize, during the study of a process zone at the tip of a propagating crack we established that upon increasing the crack velocity the zone exhibits a morphological transformation passing from a concave shape with an invagination at its back to a convex droplet-like shape. In this latter case, the metastable wake follows the propagating process zone.

ACKNOWLEDGMENT

A.L.K.'s work was supported by the RFBR under Grant No. 17-02-00365.

APPENDIX A: DERIVATION OF EQUATIONS OF MOTION

1. The Lagrangian and the dissipation function

Making use of the density of the Landau potential (3) one can write down a Lagrangian, $\mathfrak{L}$, of the solid:

$$\mathfrak{L} = \int \left\{ \frac{1}{2}\rho\left(\frac{\partial \mathbf{u}}{\partial t}\right)^2 - \Phi(\boldsymbol{\eta}, \boldsymbol{\varepsilon}) \right\} d\Omega, \tag{A1}$$

where ρ is the mass density of the solid, and Φ is the density of the Landau potential (3). We assume here that the order parameter only exhibits a relaxational dynamics and, therefore, omit the corresponding inertial term. The latter is justified at least for order-disorder phase transformations.

The equations of motion can be derived by the variation of the action $\mathfrak{A} = \int \mathfrak{L} dt$ using the Lagrangian (A1) and the dissipation function (1). One finds details on derivation of dynamic equations in [69]. One obtains the following system of equations:

$$\kappa \frac{\partial \eta}{\partial t} = g\Delta\eta - [\alpha + 2A\varepsilon_{ii}(\mathbf{R})]\eta - \beta_0\eta^3 - \gamma\eta^5, \tag{A2}$$

$$\rho \frac{\partial^2 u_i}{\partial t^2} = \frac{\partial \sigma_{ik}}{\partial X_k}. \tag{A3}$$

In this section we regard all relations in 3D. Correspondingly, the radius vector is $\mathbf{R} = (X, Y, Z)$ and the Laplace operator has the form $\Delta = \partial^2/\partial X^2 + \partial^2/\partial Y^2 + \partial^2/\partial Z^2$. The derivative of the free energy [Eqs. (3), (4), (5)] with respect to the stain, $\sigma_{ik} = \partial\Phi/\partial\varepsilon_{ik}$, represents the stress tensor:

$$\sigma_{ik} = \frac{E\sigma}{(1+\sigma)(1-2\sigma)}\varepsilon_{jj}\delta_{ik} + \frac{E}{1+\sigma}\varepsilon_{ik} + A\eta^2\delta_{ik}. \tag{A4}$$

Here δ_{ik} is the Kronecker symbol. The last term in (A4), $A\eta^2\delta_{ik}$, describes the spontaneous stress generated by the phase transition.

A general consideration with any value of the crack speed, V, one finds in [69]. In this paper for simplicity, we only consider the crack velocities, V, much slower than the speed of sound, $V \ll c$. In this case, one can approximate the mechanical equation (A3) as follows:

$$\frac{\partial \sigma_{ik}}{\partial X_k} = 0. \tag{A5}$$

We disregard changes in the temperature during the crack-zone dynamics due to the liberation or absorption of heat in the course of the phase transformation. The latter is possible, provided the heat rapidly removes from the place where it is generated or rapidly flows to the place where it is absorbed. It can happen in two cases: (i) in a material possessing a high thermal conductivity and (ii) in the case of a thin layer of material supported by a substrate with high thermal conductivity. In these cases, the temperature of the material is almost equal to the ambient temperature and Eqs. (A2) and (A5) hold. Otherwise, one needs to supplement (A2) and (A5) with the heat conduction equation. The analysis of such an extended model is, however, outside the scope of the present paper.

Equation (A2) together with Eq. (A4) constitutes the complete system of equations describing the dynamics of the process zone.

2. Elimination of the elastic variables

Degrees of freedom associated with the strain field can be eliminated using the technique of the elastic Green's function. Indeed, making use of (A5) and (A4), one can express the displacement vector u_i as

$$u_i(\mathbf{R}) = u_i^{(0)}(\mathbf{R}) - A\int G_{ij}(\mathbf{R}-\mathbf{R}')\frac{\partial \eta^2(\mathbf{R}')}{\partial X_j'}d^3R', \tag{A6}$$

where $u_i^{(0)}(\mathbf{R})$ is the displacement field generated by the crack without the transformational process zone and $G_{ij}(\mathbf{R})$ is the elastic Green's function of the solid. Einstein summation convention is assumed. Using its Fourier transform,

$$G_{ij}(\mathbf{R}) = \int G_{ij}(\mathbf{k})\exp(i\mathbf{k}\mathbf{R})\frac{d^3k}{(2\pi)^3}, \tag{A7}$$

one finds an integral representation of the dilatation $\varepsilon_{ii}(\mathbf{R})$,

$$\varepsilon_{ii}(\mathbf{R}) = \varepsilon_{ii}^{(0)}(\mathbf{R}) + A\int \eta^2(\mathbf{R}')k_ik_jG_{ij}(\mathbf{k}) \times \exp[i\mathbf{k}(\mathbf{R}-\mathbf{R}')]\frac{d^3R'd^3k}{(2\pi)^3}, \tag{A8}$$

where the crack without the process zone ($\eta \equiv 0$) engenders the strain $\varepsilon_{ii}^{(0)}(\mathbf{R})$. In the elastically isotropic case, it is given by the well-known expression

$$\varepsilon_{ii}^{(0)}(\mathbf{R}) = \frac{(1+\sigma)(1-2\sigma)K_I}{E(2\pi\rho)^{1/2}}\cos(\theta/2), \tag{A9}$$

where $\rho = \sqrt{X^2+Y^2}$ and $\theta = \arctan(Y/X)$ are the polar coordinates with the origin at the crack tip and K_I is the stress intensity factor [85]. The second term (A8) represents the contribution of the process zone to the strain. Substitution of the strain expression (A8) into (A2) yields the nonlinear, integro-differential equation of motion for the order parameter:

$$\kappa\frac{\partial\eta}{\partial t} = g\Delta\eta - \left[\alpha + 2A\varepsilon_{ii}^{(0)}(\mathbf{R})\right]\eta - \hat{N}(\eta). \tag{A10}$$

Here the nonlinear equation part, $\hat{N}(\eta)$, is expressed as follows:

$$\hat{N}(\eta) = \beta_0\eta^3(\mathbf{R}) + \gamma\eta^5(\mathbf{R}) - 2A^2\eta(\mathbf{R})\int \eta^2(\mathbf{R}')k_ik_jG_{ij}(\mathbf{k}) \times \exp[i\mathbf{k}(\mathbf{R}-\mathbf{R}')]\frac{d^3R'd^3k}{(2\pi)^3}. \tag{A11}$$

Equations (A10) and (A11) involve no elastic degrees of freedom and contain only the field $\eta(\mathbf{R})$.

One can obtain the Green's function of the solid containing a crack in two steps, as initially proposed by Bueckner [86]. During the first step, one determines the stress field in a damage-free solid to which a local force is applied. The second step determines the corresponding perturbation of the stress intensity factor due to the cut. The value of the stress obtained during the first step one determines along the cut surface, subtracts it from that originally applied [87], and finds the net stress intensity factor by the standard way. The stress field still has the universal form, $\boldsymbol{\sigma} \sim K_I\cos(\theta/2)(2\pi\rho)^{-1/2}$, where one should understand K_I as the net stress intensity factor.

The second step determines the net stress intensity factor. It involves bulky calculations, its description being lengthy. We report it elsewhere. In this paper, we describe the essential

first step, but only include step 2, by treating K_I as a net stress intensity factor.

To perform step 1, let us use (A4) and (A5) to find the elastic Green's function of the damage-free solid,

$$G_{ij}(k) = \frac{2(1+\sigma)}{E}\left[\frac{\delta_{ij}}{k^2} - \frac{1}{2(1-\sigma)}\frac{k_i k_j}{k^4}\right], \tag{A12}$$

and for (A12) the following identity holds:

$$G_{ij}(\mathbf{k})k_i k_j = -\frac{(1+\sigma)(1-2\sigma)}{E(1-\sigma)}. \tag{A13}$$

In this case, the integral in (A8) can be explicitly evaluated yielding the following relation:

$$\varepsilon_{ii}(\mathbf{R}) = \varepsilon_{ii}^{(0)}(\mathbf{R}) + \frac{A(1-2\sigma)(1+\sigma)}{2E(1-\sigma)}\eta^2(\mathbf{R}). \tag{A14}$$

With (A14), the nonlinear part (A11) of Eq. (A10) takes an especially simple form,

$$\hat{N}(\eta) = \beta\eta^3(\mathbf{R}) + \gamma\eta^5(\mathbf{R}), \tag{A15}$$

where the new negative constant $\beta < 0$ stays now instead of $\beta_0 < 0$. One expresses it in terms of the coefficients of the original Landau potential as follows:

$$\beta = -|\beta_0|\left[1 + \frac{2A^2(1-2\sigma)(1+\sigma)}{E(1-\sigma)|\beta_0|}\right]. \tag{A16}$$

One finally obtains the nonlinear dynamic equation on the order parameter (6), where $U(\mathbf{R},t) \equiv B\cos(\theta/2)\rho^{-1/2}$ accounts for the effect of the strain field on the order parameter.

As a result, we have the process zone in which $\eta(\mathbf{R},t)$ is the primary and the displacement vector, $\mathbf{u}(\mathbf{R},t)$, is the secondary order parameter. After one has solved Eq. (6), the elastic degrees of freedom can be obtained using the Green's function (A6) for $\mathbf{u}(\mathbf{R},t)$ and its derivatives.

The transformation of the integral representation (A11) into polynomial (A15) is possible due to two simplifying properties assumed in this paper. The first is the elastic isotropy of the solid proposed here. The second is that we only accounted for the spontaneous dilatation manifesting itself in the interaction term $\sim\eta^2\varepsilon_{ii}$ in the free energy density (3). If one studies an elastically anisotropic solid, or one admits shear components of the spontaneous strain, or both, the last term in $\hat{N}(\eta)$ [Eq. (A11)] does not simplify. In this case, (A10) represents the integro-differential equation. Analysis of these more complicated cases is out of the scope of this paper.

3. Automodel equation

Let us stress that this equation exhaustively describes the configuration and dynamics of the process zone at the crack tip.

Assuming that the crack propagates with the velocity V along the X axis from left to right, and expressing $\eta(X,Y,t)$ as $\eta(X-Vt,Y)$, one comes to the automodel equation in the comoving system of coordinates

$$g\Delta\eta + \kappa V\frac{\partial\eta}{\partial X'} - [\alpha - U(X',Y)]\eta - \beta\eta^3 - \gamma\eta^5 = 0. \tag{A17}$$

TABLE III. Characteristic values of the parameters of the problem.

t_0	λ_0	η_0	V_*
$\frac{\kappa g^{1/3}}{2^{1/3}B^{4/3}}$	$2^{1/3}\left(\frac{g}{B}\right)^{2/3}$	$\frac{B^{1/3}}{2^{1/6}\gamma^{1/4}g^{1/12}}$	$\frac{(2g)^{1/3}B^{2/3}}{\kappa}$

Here $X' = X - Vt$, $\Delta = \partial^2/\partial X'^2 + \partial^2/\partial Y^2$. The boundary conditions have the form $\eta|_{\partial\Omega} = 0$. The latter expresses that fact that the daughter phase only exists in the vicinity of the crack tip and vanishes away from it. Since in the following we only use the comoving system, from now on we omit the prime and write X instead of X'.

Equation (6) describes the evolution of the order parameter in the vicinity of the crack tip. In turn, (A17) treats its evolution in coordinates comoving with the velocity $V \neq 0$ of the crack.

After one has obtained the solution, $\eta(\mathbf{R},t)$, of (A17), one can use the Green's function to find the stress at the tip. The latter includes both the component generated by the crack tip itself as well as the one engendered by the process zone.

4. Rescaling

Equation (A17) depends on six parameters g, κV, α, B, β, and γ. For the numerical study, it is convenient to decrease the number of these parameters by rescaling Eq. (A17). Besides, this will make dimensionless all parameters and variables of the resulting equation. We pass from X, Y, t and the dependent variable, $\eta(X,Y,t)$, to the dimensionless ones—x, y, τ and $u = u(x,y,\tau)$—as follows:

$$\tau = t/t_0, \quad \begin{pmatrix} x \\ y \end{pmatrix} = \frac{1}{\lambda_0}\begin{pmatrix} X \\ Y \end{pmatrix}, \quad v = V/V_*, \quad u = \eta/\eta_0, \tag{A18}$$

where the expressions of the characteristic time and scale of the problem, t_0 and λ_0, the characteristic velocity, V_*, and the characteristic value of the order parameter, η_0, are summarized in Table III.

One should not confuse the rescaled order parameter, $u = u(\mathbf{r},\tau)$, that we treat here as a scalar, with the original displacement vector, $\mathbf{u}(\mathbf{R},t)$.

After these transformations Eq. (A17) transforms into Eq. (9). The latter has the form convenient for numerical solution.

APPENDIX B: TECHNICAL DETAILS OF THE SIMULATIONS

1. Relaxation method for the first-order zone

In the past, we analyzed the process zone engendered by a second-order phase transition. The latter can be described analytically in closed form, the description being asymptotically exact [69].

In contrast, no exact or asymptotically exact solution is possible in the case of a first-order zone. In this paper, we study it by numeric simulation.

We simulated the problem by the relaxation method. We formally introduced an artificial time, τ_p, referred to as the pseudotime, and assumed that $u_d = u_d(x,y,\tau_p)$. The

subscript "d" stands for "dynamic." Instead of simulating the static equation (9), we simulated the following pseudotime-dependent dynamic equation:

$$\frac{\partial u_{\rm d}}{\partial \tau_{\rm p}} = -f(u). \tag{B1}$$

One can regard the dynamics described by Eq. (B1) as the motion of a point in a functional space, the derivative, $\partial u_{\rm d}/\partial\tau_{\rm p}$, representing its velocity. One can also regard the left-hand part of (B1) as the viscous friction force with the mobility equal to unity. Its right-hand part,

$$f(u) = -\Delta u_{\rm d} - 2^{1/3} v \times \frac{\partial u_{\rm d}}{\partial x} + [a + \widetilde{U}(x,y)]u_{\rm d} - b u_{\rm d}^3 + u_{\rm d}^5, \tag{B2}$$

with the boundary condition $u_{\rm d}|_{\partial\Omega} = 0$ plays the role of a driving force in the functional space. The nonzero initial condition $u_{\rm d}(x, y, 0) = u_0(x, y) \neq 0$ is a point in this space from which the motion of the point begins.

The free energy F' (12) represents a hypersurface in the functional space. Any solution, $u_{\rm d}(x, y, \tau_{\rm p})$, of (B1) is a trajectory "drawn" on this hypersurface. If the hypersurface possesses a potential well, any trajectory falling there stops at the point of its minimum, $u_{\rm min}$. At this point the driving force vanishes:

$$f(u_{\rm min}) = 0. \tag{B3}$$

Thus, if there are several minima of the hypersurface F' they represent the fixed points of Eq. (B1).

The solution, $u(x, y)$, of the static equation (9) represents a fixed point of the dynamic equation (B1) and can be obtained as a limit: $u(x, y) = \lim_{\tau_{\rm p}\to\infty} u_{\rm d}(x, y, \tau_{\rm p})$. In practice, we approximate the function $u(x, y)$ by $u_{\rm d}(x, y, \tau_{\rm p})$ at a time $\tau_{\rm p}$ large enough to ensure convergence. This approach we have successfully applied in the past to simulate the second-order process zone [68,69,88].

In the case of the first-order zone, the situation becomes more complicated since in the hysteresis region, the hypersurface, F', has, at least, three minima, corresponding to the mother and the daughter phase zones. The latter implies that some trajectories can fall into the secondary minima, where one does not expect them.

However, the hypersurface F' of the first-order potential can have even a more complicated structure, with several secondary minima different from those of the mother and daughter phases. For example, one such secondary minimum corresponds to a solution shown in Fig. 14. It possesses straight portions of the boundary (indicated by arrows in Fig. 14), rather than the expected curved ones. The solution displayed in Fig. 14 stays in this form for a very long time of simulation exhibiting no visible evolution.

On the one hand, this implies that the solution is close to a fixed point. On the other hand, its size and the shape suggest that it is somewhere not far, but differs from the desired one. It is since the solution we are looking for is smooth. In this case, we expect it to be approximately in the form of a cardioid. One concludes that this fixed point differs from the one we look for.

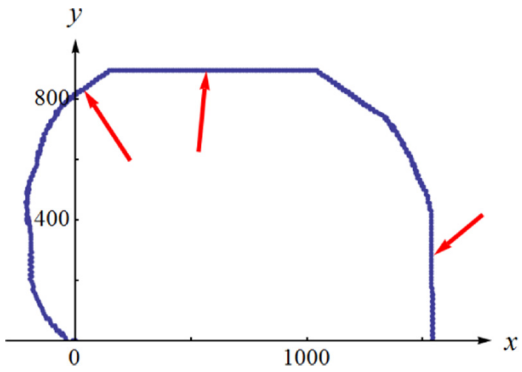

FIG. 14. The boundary of the process zone at the crack tip obtained in the simulation exhibits straight portions. The crack spans from $x = -\infty$ to $x = 0$. In the case shown here, we performed the simulation with the parameters $a = 0.22$ and $v = 0$, and the solution in this state already exhibits a good convergence which implies that the configuration corresponds to some minimum of F'. The boundary, however, exhibits straight portions indicated by arrows, suggesting that the solution is trapped in a secondary minimum.

The explanation of the fixed point shown in Fig. 14 is as follows. The straight parts of the boundary give rise to some loss of the "homogeneous" part of the energy, $\int \{[a - U(x, y)]u^2/2 - bu^4/4 + u^6/6\}dxdy$, Eq. (13). They, however, yield some energetic gain due to decreasing its "inhomogeneous" part $\int (\nabla u)^2 dxdy/2$ along the straight portions. Such an argument can be a reason for some of the secondary fixed points showing up during the relaxation method.

If the trajectory gets close to such a secondary fixed point in the functional space, it can be captured forever. Also, the hypersurface can exhibit saddle points and shallow valleys. With limited simulation time, the latter may be indistinguishable from being captured forever.

Whether or not such secondary fixed points belong to the problem under study is not a trivial question. On the one hand, the primary minimum of F' in the functional space, indeed, corresponds to the thermodynamic equilibrium. On the other hand, the secondary minima represent physical reality. Indeed, in experiments, the process zones always gradually evolve during the crack loading. The evolution is prone to be caught in the same types of secondary minima. One concludes that the relaxation approach closely mimics the experimental situation. For these reasons, the choice is open.

In this paper, we aim to study the most general properties of the wake. Hence, we only focus on the fixed points corresponding to the most pronounced minimum of the free energy, F', and leave all the secondary fixed points out. It follows that the solution corresponding to the principle minimum must have a smooth, continuous boundary. That is, the solution we are looking for should have no steps considerably exceeding the mesh size. This has been the first criterion of the selection of an acceptable solution. If we obtained a stable solution exhibiting straight boundary portions flanked by kinks or steps, we resimulated it after playing with the initial condition. We tried to guess the initial condition to be as close to the expected smooth solution as possible. In most cases after some (sometimes considerable) number of trials, we succeeded in guessing the initial shape close to the final

one, and this gave the desired smooth solution. We further controlled the convergence of such a solution—the control method we describe in the next section.

Generally, the closer we simulated to the binodal, the more difficult was the search for a smooth solution. The worst results we obtained with $a = 0.2$, such that we could not be sure that the solutions with $a = 0.2$ and $0 \leqslant v \leqslant 0.5$ were reliable. These results are not given, therefore, in this paper.

2. Software

We used the software COMSOL 5.3 for the finite-element method simulations. The dynamic system has been solved using the direct MUMPS solver with the BDF time stepping algorithm.

3. Domain

We simulated the equation of motion of a zone in the upper half plane $y \geqslant 0$ choosing a rectangular domain there, its bottom boundary being at $y = 0$. In all cases, the solution represents a plateau located in some region around the point $x = y = 0$ bounded by a kink and rapidly vanishing outside of the plateau-kink region. For this reason, the position of the other boundaries of the simulation domain was defined by trial and error, so that the solution vanishes well before the boundaries. We also set a no-flux boundary condition at the boundary $y = 0$ and the Dirichlet condition $u|_\Omega = 0$ at the rest of the rectangle boundary. By trial we have proved that provided the domain boundaries are at a certain distance from the plateau that well exceeds the kink width, their positions do not influence the solution.

As the initial condition, we used a smoothed step function, provided by COMSOL and exhibiting a smooth, narrow kink. We modified it such that it is only different from zero within either a cardioid (used for $v < v_G$) or an elongated ellipsoid (used for $v > v_G$). In the latter case, we shifted the center of the ellipsoid somewhat backward from the origin of the coordinates. These initial shapes proved to be close to the smooth final solutions and offered a reasonably fast convergence.

4. Meshing and the simulation algorithm

Part of the difficulty with this problem is its multiscaling. Indeed, the distance from the crack tip to the leading zone edge varies from a few thousand dimensionless units at low speeds to a few tens of units at high speeds, and this is also the correct estimate for the zone height. The length of the wake may achieve several thousand units. Finally, the zone interface is only a few units wide as we have seen in Fig. 12. Thus, one needs to resolve the problem on the scale of one unit and simultaneously solve the equation on the scale of a few thousand units. There is a considerable simplification in that the solution outside the zone is almost zero and is of no interest. Also within the zone, but outside of the kink, the solution is rather flat. This enabled us to try to use a mesh that is coarse away from the kink but is very fine within the kink. The difficulty here is that the position of the kink is unknown in advance. COMSOL enables a mesh with a variable size which automatically searches for the kink position and can be automatically built using the *adaptive mesh refinement* option in combination with multiple *studies*.

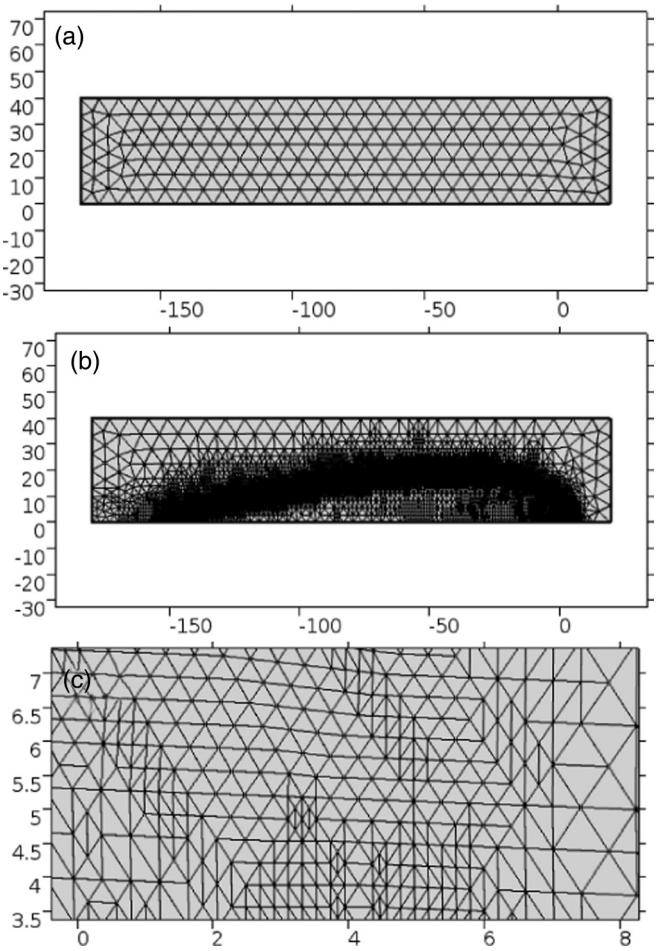

FIG. 15. Example of a mesh obtained in the course of simulation with $a = 0.23$ and $v = 0.87$. (a) The initial coarse mesh. (b) The resulting mesh after multiple refinement processes. The mesh is dense in the kink region and loose (mesh size ∼10) outside. (c) The blown-up portion of the mesh in the region of a kink showing the mesh size ∼0.1.

During each study run, the adaptive mesh refinement builds several (typically, ten) meshes as well as ten solutions employing each of these meshes. For each successive solution, it makes a new mesh determined by the value of the control function $(\nabla u)^2/10$ obtained during the previous solution process. Further, COMSOL enables one to define a new study, taking initial values from the result of the previous one. Following this procedure, one starts from a loose, homogeneous mesh, like the one shown in the upper panel of Fig. 15, and gradually comes to a highly nonhomogeneous mesh with a small mesh size in the vicinity of the kink and a loose one outside. Such a mesh is shown in the middle panel of Fig. 15. Its lower panel shows a blown-up view of the mesh part taken from the kink region. Depending on the zone size the whole process can take from several to several hundred meshes and studies.

5. Convergence control

The convergence of the solution $u_d(x, y, \tau_p)$ to $u(x, y)$ with increasing pseudotime can be controlled in different ways

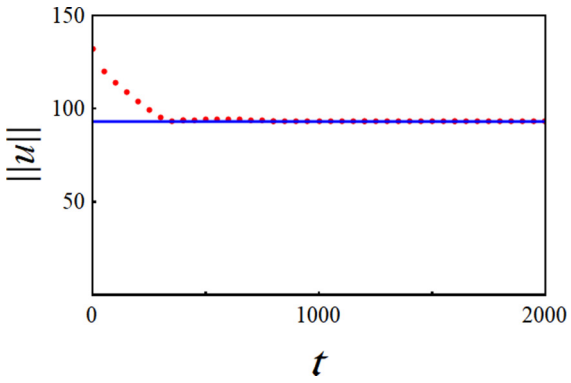

FIG. 16. Example of the convergence control of the solution. Red dots show the value of the norm (B4) obtained by the simulation (with $a = 0.24$, $b = 1$, $v = 0.6$). The solid blue line indicates the position of the horizontal asymptote.

depending on the nature of the problem. As a simple indicator, we applied the Hilbert norm, $||u||$, of the solution:

$$||u||^2 = \iint_{\Omega} u_{\mathrm{d}}^2(x, y, \tau_{\mathrm{p}}) dx dy. \tag{B4}$$

We regard the solution as having converged as soon as the norm achieves a horizontal asymptote and exhibits a variation of not more than a few percent over a time interval of several hundred dimensionless units of the pseudotime, τ_{p}. This number can vary depending on the control parameters.

Figure 16 shows an example of a good convergence for one of the simulations lasting up to 2000 pseudotime units, while the convergence has already been achieved already after about 500 ones.

6. Sampling

As a result of each simulation, we obtained two nested lists: one with the structure of the element (x, y, u), the other with the structure of $(x, y, (\nabla u)^2)$. These lists were exported from COMSOL and imported into Mathematica 11.3 for further postprocessing.

The cross section of the order parameter, $u(x, y)$, along $y = 0$ such as that shown in Fig. 6(a) was obtained from the 3D list of points with the elements (x, y, u) being those lying within a narrow strip $0 \leqslant y \leqslant y_0$, where the width of the strip, y_0, was about 100 times smaller than the zone size. Typically y_0 was 5 to 15. Then the second coordinate was left out, thus forming a list with the elements (x, u) representing the cross section.

The contours of the process zone, such as the one shown in Fig. 6(b), were obtained as follows. The data for $(\nabla u)^2$ were exported from COMSOL, yielding a list with the elements $(x, y, (\nabla u)^2)$. Such a distribution exhibits a maximum along the zone boundary, where $u(x, y)$ exhibits a steep kink. The list was reduced by selecting only those elements of the list $(x, y, (\nabla u)^2)$ for which $(\nabla u)^2$ exceeds a certain value, $(\nabla u)^2_{\max}$. Typically, $(\nabla u)^2_{\max}$ was about 0.01. This value was determined by trial and error by using interactive mechanisms of Mathematica 11.3, such as *manipulate*. Further, the elements of this reduced list were collapsed onto the (x, y) plane by $(x, y, (\nabla u)^2) \to (x, y)$, thus yielding the coordinates of the points lying close to the center of the zone boundary.

[1] D. S. Dugdale, J. Mech. Phys. Solids **8**, 100 (1960); G. I. Barenblatt, Adv. Appl. Mech. **7**, 55 (1962); G. P. Irwin, in *Proceedings of the 7th Sagamore Ordnance Materials Research Conference* (Syracuse University Research Institute, Syracuse, NY, 1960); N. S. Ottosen, M. Ristinmaa, and J. Mosler, J. Solids Struct. **53**, 70 (2015).

[2] H. Oettel and U. Martin, Int. J. Mater. Res. **97**, 1642 (2006).

[3] H. Toda, Microscopy **63**, i3 (2014).

[4] S. J. Pennycook, Ultramicroscopy **123**, 28 (2012).

[5] S. J. Wang, H. Wang, K. Du, W. Zhang, M. L. Sui, and S. X. Mao, Nat. Commun. **5**, 3433 (2014).

[6] L. R. F. Rose, Proc. R. Soc. London A **412**, 169 (1987).

[7] I. Roth *et al.*, in *ESOMAT 2009: 8th European Symposium on Martensitic Transformations*, edited by P. Sittner, V. Paidar, and H. Seiner (EDP Sciences, Les Ulis, France, 2009).

[8] S. W. Robertson *et al.*, Acta Mater. **55**, 6198 (2007).

[9] S. Daly *et al.*, Acta Mater. **55**, 6322 (2007).

[10] B. Haghgouyan, N. Shafaghi, C. C. Aydiner, and G. Anlas, Smart Mater. Struct. **25**, 075010 (2016).

[11] X. Tan *et al.*, Acta Mater. **62**, 114 (2014).

[12] F. Meschke *et al.*, J. Am. Ceram. Soc. **83**, 353 (2000).

[13] Y. H. Lu *et al.*, Intermetallics **10**, 823 (2002).

[14] S. Gollerthan, M. L. Young, A. Baruj, J. Frenzel, W. Schmahl, and G. Eggeler, Acta Mater. **57**, 1015 (2009).

[15] J. Pfetzing-Micklich, N. Wieczorek, T. Simon, B. Maass, and G. Eggeler, Mater. Sci. Eng. A **591**, 33 (2014).

[16] S. K. Hann and J. D. Gates, J. Mater. Sci. **32**, 1249 (1997).

[17] Z. Khan and M. Ahmed, J. Mater. Eng. Perform. **5**, 201 (1996); M. K. Banerjee, N. R. Bandyopadhyay, and J. Mazumder, in *Processing and Fabrication of Advanced Materials VI* (IOM Communications, London, 1998).

[18] H. F. Lopez, Mater. Lett. **51**, 144 (2001); K. Kimura, T. Asaoka, and K. Funami, in *Proceedings of the International Conference on Thermomechanical Processing of Steels and Other Materials* (TMS, Warrendale, PA, 1997), p. 1675.

[19] S. Gollerthan, M. L. Young, K. Neuking, U. Ramamurty, and G. Eggeler, Acta Mater. **57**, 5892 (2009).

[20] G. M. Loughran, T. W. Shield, and P. H. Leo, Int. J. Solids Struct. **40**, 271 (2003).

[21] H. Qiu *et al.*, Mater. Sci. Eng. A **579**, 71 (2013).

[22] L. E. Tanner, D. Schryvers, and S. M. Shapiro, Mater. Sci. Eng. A **127**, 205 (1990).

[23] U. D. Hangen and G. Sauthoff, Intermetallics **7**, 501 (1999).

[24] F. Xiong and Y. Liu, Acta Mater. **55**, 5621 (2007).

[25] F. R. Chien, R. J. Clifton, and S. R. Nutt, J. Am. Ceram. Soc. **78**, 1537 (1995).

[26] M. Song, S. Y. He, K. Du, Z. Y. Huang, T. T. Yao, Y. L. Hao, S. J. Li, R. Yang, and H. Q. Ye, Acta Mater. **118**, 120 (2016).

[27] J. A. Horton, J. L. Wright, and J. H. Schneibel, in *Bulk Metallic Glasses*, edited by W. L. Johnson, A. Inoue, and C. T. Liu (Oxford University Press, Oxford, 1999), p. 185.

[28] T. Sasaki, N. Shibata, K. Matsunaga, T. Yamamoto, and Y. Ikuhara, J. Ceram. Soc. Jpn. **120**, 473 (2012).

[29] L. Zhao, D. Bardel, A. Maynadier, and D. Nelias, Scr. Mater. **130**, 83 (2017).

[30] Y.-H. Seo, Jurij Koruza, Andreja Benčan, Barbara Malič, Jürgen Rödel, Kyle G. Webber, and C. Landis, J. Am. Ceram. Soc. **97**, 1582 (2014); C. S. Lynch, R. M. McMeeking, and Z. Suo, in *Second International Conference on Intelligent Materials*, edited by C. A. Rogers and G. G. Wallace (Technomic Publishing Co., Lancaster, PA, 1994), p. 856.

[31] S. O. Kramarov, N. Y. Egorov, and L. M. Katsnel'son, Fiz. Tverd. Tela **28**, 2858 (1986) [Sov. Phys. Solid State **28**, 1602 (1986)].

[32] V. G. Garin, Sverhtverdye materialy **2**, 17 (1982) (Superhard Materials, in Russian).

[33] A. Apte *et al.*, ACS Nano **12**, 3468 (2018).

[34] H.-J. Sue, J. D. Earls, and R. E. Hefner Jr., J. Mater. Sci. **32**, 4039 (1997).

[35] J. Karger-Kocsis and J. Varga., J. Appl. Polym. Sci. **62**, 291 (1996); S. T. Kim *et al.*, J. Mater. Sci **33**, 2421 (1998); G. A. Maier *et al.*, Macromolecules **38**, 6099 (2005); T. Koyama, T. Araki, and H. Tanaka, Phys. Rev. Lett. **102**, 065701 (2009).

[36] J. A. Donovan, Nippon Gomu Kyokaishi **75**, 239 (2002); S. Trabelsi, P.-A. Albouy, and J. Rault, Macromolecules **35**, 10054 (2002); H. P. Zhang, J. Niemczura, G. Dennis, K. Ravi-Chandar, and M. Marder, Phys. Rev. Lett. **102**, 245503 (2009); J. R. S. Martinez, X. Balandraud, E. Toussaint, J. B. Le Cam, and D. Berghezan, Polymer **55**, 6345 (2014).

[37] Y.-F. Guo and D.-L. Zhao, Mater. Sci. Eng. A **448**, 281 (2007); V. A. Borodin and P. V. Vladimirov, J. Nucl. Mater. **415**, 320 (2011); A. Latapie and D. Farkas, Modell. Simul. Mater. Sci. Eng. **11**, 745 (2003); R. Matsumoto *et al.*, Comput. Model. Eng. Sci. **9**, 75 (2005).

[38] Y. Shibutani, T. Kugimiya, and P. Gumbsch, in *Proceedings of the International Conference on Designing of Interfacial Structure in Advanced Materials and Their Joints*, edited by Masaaki Naka (Osaka University, Osaka, Japan, 2002), pp. 101–108; M. J. Buehler, H. Tang, A. C. T. van Duin, and W. A. Goddard, Phys. Rev. Lett. **99**, 165502 (2007); D. Sherman, M. Markovitz, and O. Barkai, J. Mech. Phys. Solids **56**, 376 (2008); F. Atrash and D. Sherman, *ibid.* **60**, 844 (2012); J. R. Kermode *et al.*, Nature (London) **455**, 1224 (2008); Z. Jiang, H. Fang, X. Luo, and J. Xu, Eng. Fract. Mech. **157**, 11 (2016).

[39] B. Zhang, L. Zhou, Y. Sun, W. He, and Y. Chen, Mol. Simul. **44**, 1252 (2018).

[40] J. Mei *et al.*, J. Solids Struct. **48**, 3054 (2011).

[41] M. Ruda, D. Farkas, and G. Bertolino, Comput. Model. Eng. Sci. **49**, 743 (2010).

[42] Y. Zhang *et al.*, J. Nucl. Mater. **430**, 96 (2012).

[43] A. Falvo *et al.*, J. Mater. Eng. Perform. **18**, 679 (2009).

[44] R. C. Garvi, R. H. Hannink, and R. T. Pascoe, Nature (London) **258**, 703 (1975); D. L. Porter and A. H. Heuer, J. Am. Ceram. Soc. **60**, 183 (1977); T. K. Gupta, F. F. Lange, and J. H. Behtold, J. Mater. Sci. **13**, 1464 (1978); L. K. Lenz and A. H. Heuer, J. Am. Ceram. Soc. **65**, C-192 (1982); R. P. Indel, R. W. Rice, and D. Lewis, *ibid.* **65**, c108 (1982); N. Claussen, Z. Werkstofftechnik **13**, 138 (1982); F. F. Lange, J. Mater. Sci. **17**, 240 (1982); P. F. Becher and V. J. Tennery, in *Fracture Mechanics of Ceramics*, edited by R. C. Bradt (Plenum, New York, 1983), Vol. 6, p. 383.

[45] P. M. Kelly and L. R. F. Rose, Prog. Mater. Sci. **47**, 463 (2002).

[46] I. Birkby and R. Stevens, Key Eng. Mater. **122–124**, 527 (1996).

[47] R. I. Todd and M. P. S. Saran, in *Materials Processing Handbook*, edited by J. R. Groza (CRC Press, Boca Raton, FL, 2007), Chap. Transformation Toughening.

[48] N. Nishiyama *et al.*, Sci. Rep. **4**, 6558 (2014).

[49] C. Wuenshe, E. Raedlein, and G. H. Frischat, Glastech. Ber. Glass Sci. Techol. **72**, 4954 (1999).

[50] M. Takeda *et al.*, J. Elect. Microscopy **48**, 609 (1999); K. Youssef, P. Kulshreshtha, and G. Rozgonyi, Photovoltaics for the 21st Century **25**, 49 (2010); P. K. Kulshreshtha, K. M. Youssef, and G. Rozgonyi, Solar Energy Mater. Solar Cells **96**, 166 (2012).

[51] I. Brough, R. N. Haward, G. Healey, and A. Wood, Polymer **45**, 3115 (2004).

[52] K. Tozawa *et al.*, J. Elect. Microscopy **48**, 613 (1999).

[53] E. Hornbogen, Acta Metall. **26**, 147 (1978).

[54] D. Hennessy, G. Steckel, and C. Altstetter, Met. Trans. A **7**, 415 (1976).

[55] J. E. Huber, F. Hofmann, S. Barhli, T. J. Marrow, and C. Hildersley, Scr. Mater. **140**, 23 (2017).

[56] C. J. Gilbert, V. Schroeder, and R. O. Ritchie, in *Bulk Metallic Glasses*, edited by W. L. Johnson, A. Inoue, and C. T. Liu (Material Res. Soc., Warrendale, PA, 1999), p. 34.

[57] A. A. Bulbich, J. Mater. Sci. **27**, 1070 (1992).

[58] J. S. Kim *et al.*, Met. Mater. Int. **14**, 165 (2008).

[59] R. M. McMeeking and A. G. Evans, J. Amer. Ceram. Soc. **65**, 242 (1982).

[60] B. Budiansky, J. W. Hutchinson, and J. C. Lambropoulos, Int. J. Solids Struct. **19**, 337 (1983).

[61] S. D. Antolovich, Trans. Met. Soc. AIME **242**, 2371 (1968).

[62] S. D. Antolovich and D. Fahr, Eng. Fract. Mech. **4**, 133 (1972).

[63] N. Simha and L. Truskinovsky, Acta Metall. Mater. **42**, 3827 (1994).

[64] J. Fineberg and M. Marder, Phys. Rep. **313**, 1 (1999); C.-H. Chen, E. Bouchbinder, and A. Karma, Nat. Phys. **13**, 1186 (2017).

[65] A. Boulbitch and A. L. Korzhenevskii, Phys. Rev. Lett. **107**, 085505 (2011).

[66] A. Boulbitch and A. L. Korzhenevskii, Europhys. Lett. **112**, 16003 (2015).

[67] A. Boulbitch and A. L. Korzhenevskii, Phys. Rev. E **93**, 063001 (2016).

[68] A. Boulbitch and A. L. Korzhenevskii, Eur. J. Phys. B **89**, 261 (2016).

[69] A. Boulbitch, Yu. M. Gufan, and A. L. Korzhenevskii, Phys. Rev. E **96**, 013005 (2017).

[70] A. A. Boulbitch and A. L. Korzhenevskii, Europhys. Lett. **123**, 16003 (2018).

[71] E. Y. Tonkov, *High Pressure Phase Transformations: A Handbook* (Gordon and Breach, Amsterdam, 1992).

[72] A. L. Roitburd, Sov. Phys. Usp. **17**, 326 (1974).

[73] A. Boulbitch and A. L. Korzhenevskii, Phys. Rev. E **101**, 033004 (2020).

[74] L. D. Landau and E. M. Lifshitz, *Statistical Physics*, 3rd ed. (Pergamon Press, Oxford, 1985).

[75] J. C. Toledano and P. Toledano, *The Landau Theory of Phase Transitions* (World Scientific, Singapore, 1987).
[76] L. B. Freund, *Dynamic Fracture Mechanics* (Cambridge University Press, Cambridge, 1998).
[77] Yu. M. Gufan, *Structural Phase Transitions* (Nauka, Moscow, 1983) (in Russian).
[78] V. P. Dmitriev, S. B. Rochal, Y. M. Gufan, and P. Toledano, Phys. Rev. Lett. **60**, 1958 (1988).
[79] P. Toledano and V. Dmitriev, Reconstructive phase transitions, *Crystals and Quasicrystals* (World Scientific, Singapore, 1996).
[80] S. J. Wang *et al.*, Sci. Rep. **3**, 3102 (2013).
[81] V. P. Sakhnenko and V. M. Talanov, Sov. Phys. Solid State **21**, 1401 (1979); **22**, 458 (1980).
[82] H. M. Ledbetter and R. P. Reed, J. Phys. Chem. Ref. Data **2**, 531 (1973); W. F. Weston and A. W. Granato, Phys. Rev. B **12**, 5355 (1975); Y. K. Yogurtcu and G. A. Saunders, Philos. Mag. **52**, 833 (1985); A. S. Johal and D. J. Dunstan, Phys. Rev. B **73**, 024106 (2006).
[83] A. Karma, D. A. Kessler, and H. Levine, Phys. Rev. Lett. **87**, 045501 (2001); V. Hakim and A. Karma, *ibid.* **95**, 235501 (2005); R. Spatschek, M. Hartmann, E. Brener, H. Mueller-Krumbaar, and K. Kassner, *ibid.* **96**, 015502 (2006).
[84] L. Q. Chen, in *Physics of Ferroelectrics: A Modern Perspective*, edited by K. M. Rabe, C. H. Ahn, and J. M. Triscone (Springer, Berlin, 2007), pp. 363–371.
[85] N. F. Morozov, *Mathematical Problems of the Theory of Cracks* (Nauka, Moscow, 1984) (in Russian).
[86] H. F. Bueckner, Trans. ASME **80**, 1225 (1958).
[87] N. I. Muschelisvili, *Some Basic Problems of the Mathematical Theory of Elasticity* (Noordoff, Groningen, 1963).
[88] A. Boulbitch, Mathematica J. **20**, 1 (2018).